

REPORT DOCUMENTATION PAGE			Form Approved OMB No. 0704-0188	
Public reporting burden for this collection of information is estimated to average 1 hour per response, including the time for reviewing instructions, searching existing data sources, gathering and maintaining the data needed, and completing and reviewing the collection of information. Send comments regarding this burden estimate or any other aspect of this collection of information, including suggestions for reducing this burden, to Washington Headquarters Services, Directorate for Information Operations and Reports, 1215 Jefferson Davis Highway, Suite 1204, Arlington, VA 22202-4302, and to the Office of Management and Budget, Paperwork Reduction Project (0704-0188), Washington, DC 20503.				
1. AGENCY USE ONLY (Leave blank)		2. REPORT DATE June 1, 2003		3. REPORT TYPE AND DATES COVERED SBIR Final Report – Oct.2, 2002 thru Jun.1, 2003
4. TITLE AND SUBTITLE Deep Ultraviolet Laser Diode for UV -Resonance Enhanced Raman Identification			5. FUNDING NUMBERS ARPA Order K475/66,	
6. AUTHORS W. Hug, T.Moustakas, R.Treece, J.Smith, A.Bhattacharyya, R.Reid, J.Pankove			Contract No. DAAH01-03-C-R015, PAN RTW 20-03	
7. PERFORMING ORGANIZATION NAME(S) AND ADDRESS(ES) Photon Systems 1512 Industrial Park St. Covina, CA 91722			8. PERFORMING ORGANIZATION REPORT NUMBER 2002 DARPA, Ph.I,SBIR, Rept.No2	
9. SPONSORING/MONITORING AGENCY NAME(S) AND ADDRESS(ES) U.S. Army Aviation & Missile Command AMSAM-AC-RD-AY Linda Norwood, (256) 876-8918 Redstone Arsenal, AL 35898-5280			10. SPONSORING/MONITORING AGENCY REPORT NUMBER	
11. SUPPLEMENTARY NOTES				
12a. DISTRIBUTION/AVAILABILITY STATEMENT Unclassified			12b. DISTRIBUTION CODE	
13. ABSTRACT (Maximum 200 words) <p>This proposal addresses the need for deep UV semiconductor lasers for use in UV resonance enhanced Raman spectroscopic identification of biological agents. The proposed approach avoids the problems of p-doping and ohmic contacts by using subminiature direct electron injection excitation of an InAlGa_N heterostructure. We have demonstrated strong stimulated emission at 274nm using this approach with measured linewidth reduction from 16nm to 4nm and five orders of magnitude non-linear increase in intensity.</p> <p>High levels of chemical specificity can be obtained using Raman spectroscopy without sample preparation, contact, or destruction. When Raman excitation occurs within the electronic resonance band of a material the scatter cross-sections can improve as much as eight orders of magnitude. For biochemical molecules such as nucleic and amino acids these absorption bands are very strong in the deep UV between about 220nm and 280nm. When Raman excitation is below about 250nm, there is a fluorescence-free region extending over 4000 wave numbers above the excitation wavelength providing very high detection sensitivities and low background noise.</p> <p>It is the goal of this proposed program to demonstrate deep UV emission from a semiconductor laser and the ability to obtain deep UV resonance Raman spectra of analogs of hazardous biological agents.</p>				
14. SUBJECT TERMS deep UV semiconductor laser Raman spectroscopy biological agent detection			15. NUMBER OF PAGES 64	
			16. PRICE CODE FFP	
17. SECURITY CLASSIFICATION OF REPORT Unclassified	18. SECURITY CLASSIFICATION OF THIS PAGE Unclassified	19. SECURITY CLASSIFICATION OF ABSTRACT Unclassified	20. LIMITATION OF ABSTRACT Unlimited	

NSN 7540-01-280-5500
FORM 298 (Rev 2-89)

Computer Generated

STANDARD

Prescribed by ANSI Std Z39-18

298-102

PHOTON
S Y S T E M S

20030612 158

"Deep Ultraviolet Laser Diode for UV-Resonance Enhanced Raman Identification
of Biological Agents"

**Final Report
June 1, 2003**

Sponsored by
Defense Advanced Research Projects Agency (DOD)
(Controlling DARPA Office)

ARPA Order K475/66

Issued by U.S. Army Aviation and Missile Command Under

Contract No. DAAH01-03-C-R015

William F. Hug, Ph.D. Principal Investigator
Tel: 626 967-6431
w.hug@photonsystems.com

Photon Systems, Inc.
1512 Industrial Park St.
Covina, CA 91722-3417
www.photonsystems.com

"ESUVOS Development"
Effective Date of Contract: October 2, 2002

Contract Expiration Date: April 2, 2003

"The views and conclusions contained in this document are those of the authors
and should not be interpreted as representing the official policies, either
expressed or implied, of the Defense Advanced Research Projects Agency of the
U.S. Government."

UNCLASSIFIED
"Approved for public release; distribution unlimited"

1.0	Table of Contents	3
2.0	Abstract	4
3.0	Technical Discussion	5
3.1	Executive Summary	5
3.2	Introduction	7
3.3	Summary Description of Tasks	8
3.4	Status of ESUVOS Development	10
3.4.1.	Overview of ESUVOS concept	10
3.4.2	AlGaIn materials development, characterization and processing	12
	Overview	12
	Bulk materials	15
	MQW structures	19
	GRINSCH structures	22
	Stimulated emission results	27
	Processing of faceted laser dies	31
	Stripe/mesa photomask design and fab	31
	Stripe/mesa photolithography & facet etch	34
	Preliminary characterization of faceted samples	36
	Summary of materials results	37
3.4.3	Electron source design	38
3.4.4	Electrostatic e-beam focusing	39
3.4.5	SUVOS packaging	44
3.4.6	ESUVOS power supply	46
3.4.7	Laboratory test bed	48
3.5	Optical Detection and Identification of Biological Agents	50
3.5.1	Background	51
3.5.2	UV resonance fluorescence classification of bioagents	51
3.5.3	UV Raman identification of bioagents	56
	Taxonomic Raman marker bands	57
	Biological agent identification specificity	61
	UV MicroRaman Instrument: general specifications	63
4.0	Conclusions and Recommendations	63
	Distribution List	64

2.0 Abstract

In general, this report addresses the need for low false alarm rate, non-contact methods for detection and identification of biological agents such as bacterial spores. In particular, this report addresses the need for deep UV semiconductor lasers for use in UV resonance enhanced Raman spectroscopic identification of biological agents. The proposed approach avoids the problems of p-doping and ohmic contacts by using subminiature direct electron injection excitation of an InAlGaN heterostructure. Using this concept, we have demonstrated stimulated emission at 274nm from AlGaIn bulk material with 72% aluminum content. We observed five orders of magnitude increase in CL intensity for an increase of only two orders of magnitude in pump current and a corresponding narrowing of the spectral line from 16nm to 4 nm

High levels of chemical specificity can be obtained using Raman spectroscopy without sample preparation, contact, or destruction. When Raman excitation occurs within the electronic resonance band of a material the scatter cross-sections can improve as much as eight orders of magnitude. For organic molecules such as nucleic acids and amino acids and other biochemicals these absorption bands are very strong in the deep UV between about 220nm and 280nm. In addition, when Raman excitation below about 250nm is employed, there is a fluorescence-free region extending over 4000 wave numbers above the excitation wavelength providing very high detection sensitivities and low background noise.

It is the goal of this proposed program to demonstrate deep UV emission from a semiconductor laser and the ability to obtain deep UV resonance Raman spectra of analogs of hazardous biological agents.

Anticipated Benefits/Potential Commercial Applications of the Research or Development

The Electron-beam Semiconductor UltraViolet Optical Source (ESUVOS) being developed here will enable a revolutionary reduction in size, weight and power consumption for UV resonance Raman and laser induced native fluorescence instruments for the detection and classification of biological agents on surfaces, in water and in the air.

In addition, there is a broad commercial market need for deep UV sources that are small and efficient. The largest of these markets is likely in optical memory systems where the aerial data density is inversely proportional to the square of the source emission wavelength. However, other markets, while potentially smaller in quantity of demand, may have greater overall commercial impact, being the enabling technology for a wide array of analytical instruments. These instruments include biotechnology instruments used in clinical diagnostics, pharmaceutical research and product testing; environmental monitoring such as water, air and food quality; in semiconductor development and processing, and a myriad of other applications where small spot sizes or photon-energy-specific excitation is needed or enabling.

List a maximum of 8 Key Words that describe the Project.

Ultraviolet, semiconductor, laser, resonance, Raman, spectroscopy, biological

3.0 Technical Discussion

3.1 Executive Summary

The general goal of this program is development of components and associated instruments for the detection and identification of biological agents used in bioterrorism. Several integrated instruments are needed which start with very high sensitivity, low specificity methods, progressing to methods with higher levels of specificity with a sacrifice in sensitivity. The initial instrument will likely use laser induced resonance (native) fluorescence to provide the first level of detection and discrimination, enabling detection of single microorganisms and classification of particles into broad biologic and non-biologic categories. The second instrument will likely be based on UV resonance Raman spectroscopy, enabling further classification into Gram-type, spore or non-spore, and basic cellular composition. The time constant for these two measurements will likely be less than a second (and potentially less than a microsecond). Higher levels of specificity can also be accomplished using UV resonance Raman with higher spectral resolution, but this may take tens of seconds to achieve improved identification. Target particles that continue to merit further analysis will likely be passed to other instrument modalities such as DNA-sequence-based instruments for measurements to even higher levels of specificity. This is the context in which the present Phase I SBIR program is set.

The primary goal of this Phase I SBIR has been to demonstrate the feasibility of producing a Semiconductor Ultra-Violet Optical Source (SUVOS) in a subminiature package using an electron beam to avoid the traditional problems of p doping and ohmic contacts associated with pn junction devices. We call this device an ESUVOS. The goals of this Phase I SBIR have been achieved.

In the work discussed below we have shown the feasibility of fabricating an ESUVOS laser for operation in the 220 nm to 250 nm region of the deep UV and of creating a manufacturing flow to make large numbers of the devices. The feasibility of fabricating an ESUVOS laser was shown in our Phase I program through advancements in optical results, materials growth, stripe processing, and device design/packaging summarized in the following list of milestones:

- Production of stimulated emission at 274 nm from the surface of an $\text{Al}_{0.72}\text{Ga}_{0.28}\text{N}$ alloy (bulk material) as shown by
 - a. A superlinear increase in CL intensity as a function of probe current above a threshold value of approximately 4×10^{-8} Amps. Overall, a five orders of magnitude increase in CL intensity was observed for an increase of only two orders of magnitude in probe current.
 - b. Narrowing of the CL line width from 16 to 4 nm as a function of increasing probe current.
- Demonstration of the ability to grow uniform multiple quantum well (MQW) alloys ($\text{Al}_y\text{Ga}_{1-y}\text{N}/\text{Al}_x\text{Ga}_{1-x}\text{N}$).
- CL emission at 222 nm from a MQW sample.

- Demonstration of the ability to grow Graded Index Separate Confinement Heterostructures (GRINSCH) incorporating a double heterostructure as the active region.
- Processing of laser stripes on $\text{Al}_x\text{Ga}_{1-x}\text{N}$ material via the CAIBE etch technique.
- Acquisition of a miniature electron beam source suitable for the ESUVOS vacuum envelope from a commercial vendor.
- Design and fabrication of a miniature vacuum envelope for housing the electron source, ebeam optics, and a faceted UV laser die.

The central achievement in this work was the demonstration of strong stimulated emission from an ESUVOS. To the best of our knowledge, this is the shortest wavelength at which stimulated emission has ever been demonstrated from a semiconductor device.

In addition, we have completed the design and begun fabrication of parts for an ESUVOS device with size less than about 2 cubic centimeters in volume. All of the basic components, including the diamond microtip field emission cold cathode electron source, the electrostatic e-beam focusing lens design, the AlGa_N materials, and the power supply are available, showing that this pragmatic approach to achieving a sub-miniature deep UV semiconductor source will prove successful.

Although the goals of the Phase I effort were largely focused on the development of the ESUVOS device, the ultimate goal of using this device for UV resonance Raman spectroscopic identification of bioterrorism organisms has continued as well. Details of the UV resonance Raman application of an ESUVOS device in a bioterrorism organism detector will be discussed in Section 3.5 of this report. ***We have demonstrated the efficacy of using an ESUVOS source for UV resonance Raman spectroscopic identification of microorganisms. Furthermore, we have developed an ultra sensitive UV Raman detection instrument and spectroscopic decision tree which can enable a sub-500cc instrument capable of identification of small quantities of biological agents with a high level of specificity. The instrument can clearly identify Gram type, spore configuration, and G+C content to identify biological agents. This is also described in Section 3.5***

This Phase I SBIR program is a collaboration between several groups including **Photon Systems** (Thomas Duprez, David Cooper), **Astralux** (Jacques Pankove, Rande Treece, Jim Smith, Deepak Sengupta), **Boston University** (Theodore Moustakas, Anirban Bhattacharyya), the **U.S. Naval Research Laboratory** (Jon Shaw), and **Extreme Devices** (Ben Tao).

3.2 Introduction

In general, this report addresses the need for low false alarm rate, non-contact methods for detection and identification of biological agents such as bacterial spores. In particular, this report describes the development of deep UV semiconductor lasers and their use in UV resonance enhanced Raman and laser induced resonance fluorescence spectroscopic detection and identification of biological agents.

Photon Systems and other organizations are proposing a variety of optical techniques for in situ, non-contact, detection and identification of biological warfare agents. Optical techniques are being proposed because they require no sample preparation or handling and are generally easy to use and rapid compared to wet-chemistry techniques presently being employed. Among the techniques being proposed is UV resonance (native) fluorescence, UV resonance Raman and coherent anti-stokes Raman spectroscopy¹.

The ability to optically discriminate microbes from complex backgrounds and classify them, with low false alarm rates, depends on the ability of a proposed technique to accurately measure and relate spectroscopic chemical signatures to essential features of the microbes under investigation. This ability depends strongly on the excitation and observation wavelengths employed, which is true for all optical techniques being proposed. Our focus is on laser induced UV resonance Raman and resonance fluorescence spectroscopy because we believe these techniques are the only viable high-sensitivity techniques that could be deployed in low power, miniature, robust, and inexpensive packages.

Miniature, semiconductor UV optical sources (SUVOS's) emitting in the 220nm to 250nm wavelength range are *the* key enabling technology for a new generation of micro-miniaturized UV-enhanced resonance Raman and resonance fluorescence-based sensors and instruments for non-contact, in situ, detection and identification (without the need for sample preparation) of a wide range of biological materials including weaponized biological agents. Although significant efforts are underway to develop InAlGaN pn junction diodes that emit at wavelengths as low as 280nm, ***shorter excitation wavelengths are needed to enable resonance-enhanced Raman detection of critical cellular chemicals without interference from background fluorescence.***

Successful development of these SUVOS's will enable dramatic improvements in a wide range of commercial as well as governmental applications. Commercial applications include much higher density CDROM's, new instruments for medical clinical diagnostics, faster and simpler DNA sequencers, new and better instruments for environmental testing, food and pharmaceutical testing and many research applications. Governmental

¹ Scully, M.O., et.al., "FAST CARS: Engineering a laser spectroscopic technique for rapid identification of bacterial spores", PNAS, Vol.99, No.17, pp.10994-11001, Aug. 20, 2002

applications include revolutionary improvements in instruments for detection of biological and chemical weapons, bomb residue detection and identification, illegal drug residue sensors as well as a broad range of research applications including discovery of life outside Earth and better understanding life on Earth.

Major technical roadblocks have impeded development of pn-junction-based semiconductor UV optical sources (SUVOS). These roadblocks include the difficulty of p-doping high aluminum content AlGa_N materials and the inability to make ohmic contacts to these materials. This is especially true for deep UV sources below 300nm that require greater than about 35% aluminum content. The goal of this Phase I SBIR program is to demonstrate feasibility of a direct, pragmatic, approach that avoids these traditional problems by using subminiature direct electron injection excitation of an AlGa_N semiconductor heterostructure. We call this approach an ESUVOS for Electron-beam pumped Semiconductor Ultra-Violet Optical Source.

Prior to this SBIR program we demonstrated cathodoluminescence emission at 238nm using this concept from AlGa_N bulk material with 87% aluminum content. During this Phase I SBIR program we have demonstrated strong stimulated emission at 274nm with 72% aluminum content. We observed a nonlinear increase of the intensity by about five orders of magnitude as the pump current is increased by two orders of magnitude and a corresponding narrowing of the spectral line from 16nm to 4 nm. This Phase I SBIR has focused on our ESUVOS path to achieving deep UV emission from both LED and laser devices which can be nearly the size of typical pn junction semiconductor devices. In addition, we have made significant progress in developing ultra-miniature and ultra-sensitive UV resonance Raman instrumentation and detection modes to both detect and identify biological agents using this non-contact, non-destructive, hands-off technique.

3.3 Summary Description of Tasks

To achieve the goals of this Phase I effort we have planned the following seven tasks. We have gone beyond these original tasks during the Phase I effort, but include the original tasks here for completeness.

Task 1. Overall Design. This task is to develop an ESUVOS device design compatible with an LED and laser configuration. In this task we plan to develop the electrical, optical and mechanic specifications for the major components of the ESUVOS including the micro e-beam source, the e-beam confinement method/s, the AlGa_N structure and substrate configuration and the vacuum packaging. Discussed in Sections 3.4.1, 3.4.3, 3.4.4, and 3.4.5 of this report.

Task 2. Electron Beam Source. This task is to fabricate and/or procure a micro e-beam source compatible with above device design. Sample AlGa_N

target materials will be used to evaluate electron flux on the target. This is discussed in Section 3.4.3 of this report.

Task 3. AlGaIn Material Growth & Characterization. This task is to grow bulk and/or multiple quantum well AlGaIn material in a form compatible with the above demonstration device. We will begin by using AlGaIn bulk material provided by Boston University to build the first demonstration LED devices. Later in the Phase I we expect to receive MQW materials in a configuration compatible with the end device. Discussed in Section 3.4.2 of this report.

Task 4. ESUVOS LED Fabrication. This task is to fabricate and test a demonstration miniature deep UV LED device. This task will integrate all of the elements into a final demonstration LED device. This is discussed in Sections 3.4.2, 3.4.5 and 3.4.7 of this report.

Task 5. ESUVOS Laser Design. This task is to refine the design for a laser version of the ESUVOS. This will take into account all that has been learned regarding optimization of the e-beam source, e-beam focusing "optics", MQW structure and overall package design compatible with mass production. This is discussed in Section 3.4.5 of this report.

Task 6. UV Raman Data. This task is to take representative UV resonance Raman spectra of anthrax analog samples with excitation wavelength near 225nm and 250nm. This is discussed in Section 3.5 of this report.

Task 7. Final Report. This task is to prepare one final report.

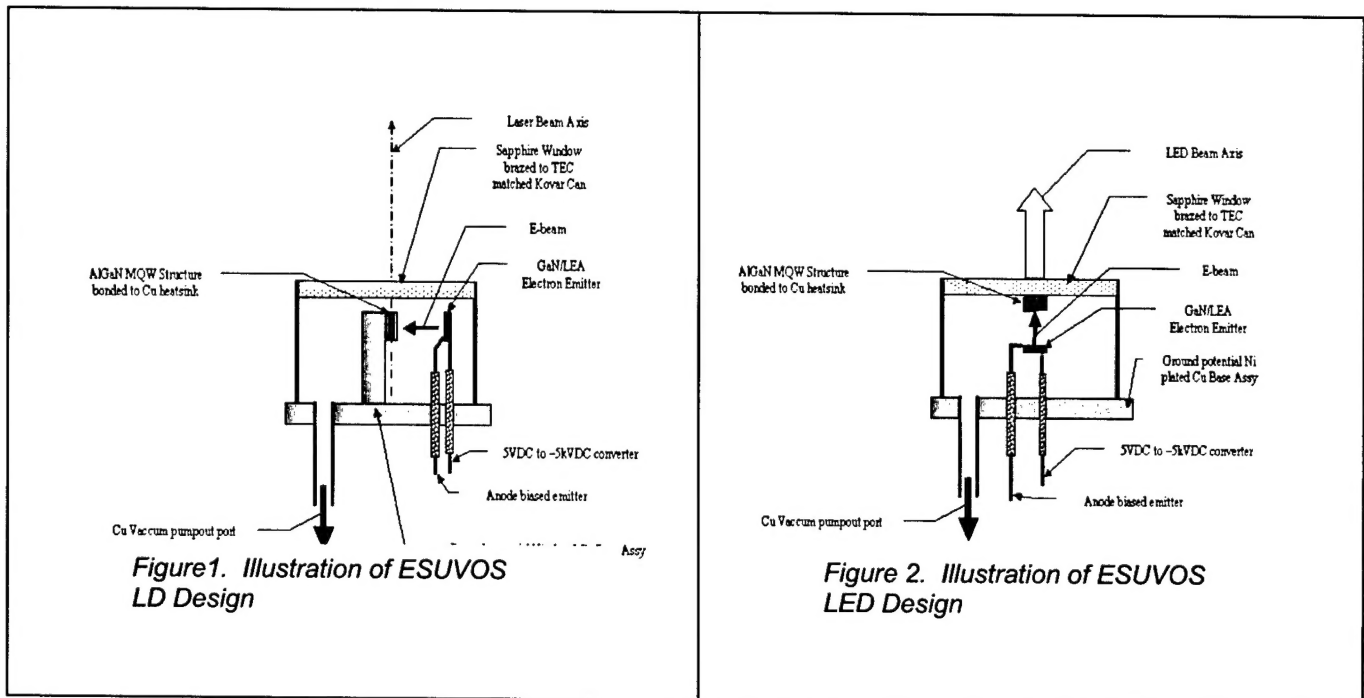
Phase I SBIR Task Plan

	Months					
	1	2	3	4	5	6
1. Develop ESUVOS device design		♦				
2. Fabricate and/or procure e-beam source			♦			
3. Grow AlGaIn sample compatible with device					♦	
4. Fabricate ESUVOS LED version of device						♦
5. Develop refined design for laser version of ESUVOS					♦	
6. Take URRRS data on anthrax analog organisms						♦
7. Final Report						♦

3.4 Status of ESUVOS Development

3.4.1 Overview of ESUVOS Concept and Phase I Milestones

The original, proposed, concept for laser diode (LD) and light emitting diode (LED) versions of the ESUVOS are illustrated, respectively in Figs. 1 and 2 below.



The fundamental concept is to enclose an electron source, an electrostatic focusing electrode, an AlGaIn UV emitter, and an anode in a miniature vacuum envelope. The current design concept is illustrated in Fig. 3, below.

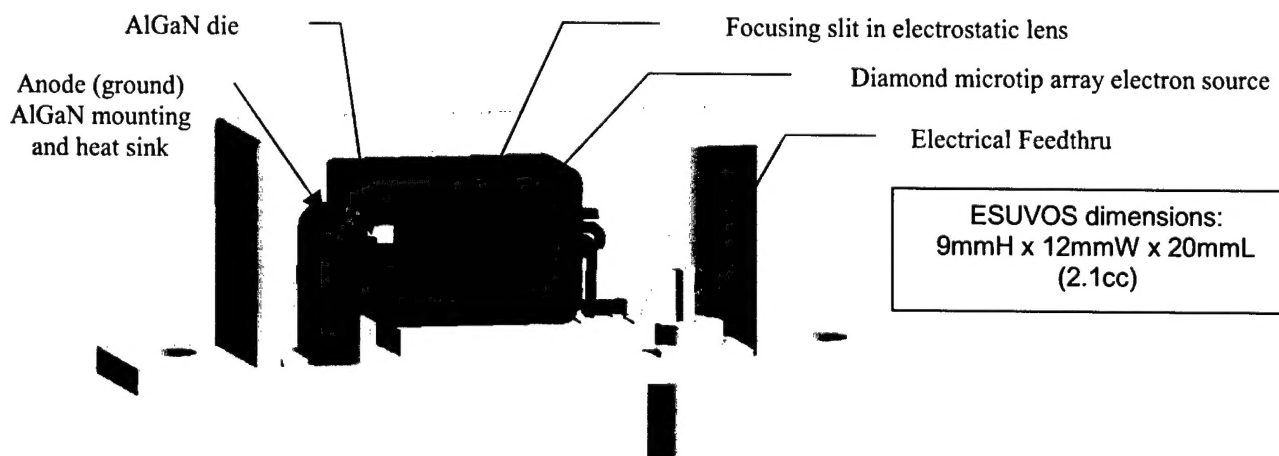


Figure 3. Cross-section of ESUVOS laser device

UV emission from the device is via an optical window or optical fiber pigtail. The construction and processing methods are similar to traditional optoelectronic butterfly packaging, where vacuum environments are often used for high impedance CMOS devices.

The feasibility of fabricating an ESUVOS laser was shown in our Phase I program through advancements in optical results, materials growth, stripe processing, and device design/packaging summarized in the following list of milestones:

- Production of stimulated emission at 274 nm from the surface of an $\text{Al}_{0.72}\text{Ga}_{0.28}\text{N}$ alloy (bulk material) as shown by
 - b. A superlinear increase in CL intensity as a function of probe current above a threshold value of approximately 4×10^{-8} Amps. Overall, a five orders of magnitude increase in CL intensity was observed for an increase of only two orders of magnitude in probe current.
 - b. Narrowing of the CL line width from 16 to 4 nm as a function of increasing probe current.
- Demonstration of the ability to grow uniform multiple quantum well (MQW) alloys ($\text{Al}_y\text{Ga}_{1-y}\text{N}/\text{Al}_x\text{Ga}_{1-x}\text{N}$).
- CL emission at 222 nm from a MQW sample.
- Demonstration of the ability to grow Graded Index Separate Confinement Heterostructures (GRINSCH) incorporating a double heterostructure as the active region.
- Processing of laser stripes on $\text{Al}_x\text{Ga}_{1-x}\text{N}$ material via the CAIBE etch technique.
- Acquisition of a miniature electron beam source suitable for the ESUVOS vacuum envelope from a commercial vendor.
- Design and fabrication of a miniature vacuum envelope for housing the electron source, ebeam optics, and a faceted UV laser die.

Each of these milestones in ESUVOS development is discussed further below.

3.4.2 AlGa_N Mat'ls Development, Characterization, and Processing Overview

Electroluminescent laser diodes (LDs) operating at wavelengths as short as about 390 nm,^{2,3,4,5} as well as light emitting diodes (LEDs) operating at wavelengths into the UV as far as 333 nm⁶ have been fabricated using alloys of the III nitrides in QW and multiple quantum well (MQW) structures. MQW structures have been shown by Nakamura and others to be very important to achieving stimulated emission in the III-nitrides. Nakamura used conventional metal contacts and stimulated emission through the p-n diode. The Japanese group at Riken has made LEDs operating down to 333 nm by pushing the Al content of the AlGa_N alloys to 25 %. The challenge to reducing the emission wavelength further for electroluminescent devices is the inability to make Al-rich AlGa_N sufficiently conducting to allow for electronic current injection.

However, in the approach we are pursuing here, our deep UV lasers employ electron pumping via ballistic electron injection into the QW. Molva et al. demonstrated lasing at 825 nm, 763 nm, 753 nm, and 478 nm from electron pumped graded QW Ga_xAl_{1-x}As, Cd_xMn_{1-x}Te, , Cd_xMn_{1-x}Te, and Zn_xCd_{1-x}Te, respectively. Molva proved the feasibility of this approach by pumping the QW II-VI and III-V materials using a field emitter array as an electron source and packaging the entire laser in a miniature vacuum package. He developed miniature electron optics to focus the emitted electrons onto the semiconductor lasing material.

Although it has been believed necessary to use QW or MQW structures to achieve stimulated emission, we have achieved it in bulk material without mirror facets. The Riken group has demonstrated photoluminescence (PL) at 220 nm from bulk AlGa_N (with 95% Al) films and PL at 229 nm from MQW samples (well composition of Al_{0.18}Ga_{0.82}N, and barrier of AlN)⁷. Their results show that the PL from MQWs were several tens of times greater than the PL from the bulk samples.

Indium will be added to the AlGa_N alloys to improve the materials quality. Increasing concentration of Al in AlGa_N, although necessary to increase the band gap, also leads to increased built-in electric fields related to strain and spontaneous polarization.⁸ Through the addition of a small amount of indium (In) to the AlGa_N alloy, thereby creating a quaternary alloy, AlInGa_N, it is possible to engineer the strain.⁹ AlInGa_N materials have been shown to form

² S. Nakamura, et al., *Jpn. J. Appl. Phys.*, Part 2 **38**, L226 (1999).

³ S. Nakamura, et al., *Jpn. J. Appl. Phys.*, Part 1 **30**, 1620 (1991).

⁴ S. Nakamura, et al., *Appl. Phys. Lett.*, **76**, 22 (2000).

⁵ S. Kawakami, et al., *Appl. Phys. Lett.*, **77**, 2151 (2000).

⁶ A. Kinoshita, et al., *Appl. Phys. Lett.*, **77**, 175 (2000).

⁷ H. Hirayama, et al., *MRS Internet J. Nitride Semicond. Res.* **5S1**, W11.35 (2000).

⁸ T. Takeuchi, et al., *Appl. Phys. Lett.* **73**, 1691 (1998).

⁹ M. Asif Khan, et al., *Appl. Phys. Lett.* **76**, 1161 (2000).

high-quality p-n junctions ¹⁰ and MQWs for bright UV ¹¹ and blue LEDs ¹². Adding In to AlGa_N barriers in InGa_N-Al(In)Ga_N MQWs resulted in a significant increase in PL intensity compared to InGa_N-AlGa_N MQWs. ¹³.

The core of this new deep UV laser is the AlGa_N semiconductor structure. A total of 11 wafers have been processed to evaluate aspects of the semiconductor design. These wafers are listed in Table I below. A range of bulk (homogeneous) material with and without facets, multiple quantum well materials, and GRIN-SCH structures were produced. Not all of this material has been fully characterized to date. Five (5) wafers were grown as homogeneous bulk material with various aluminum concentrations. These were samples 896, 898, 1066, 1278 and 1281. Four (4) wafers were grown with multiple quantum wells. These were 1283, 1285, 1286 and 1289. And finally, two wafers were grown with a GRIN-SCH structure, 1303 and 1304.

¹⁰ A. Chitnis, et al., *Appl. Phys. Lett.* **77**, 3800 (2000).

¹¹ V. Adivarahan, et al., *Appl. Phys. Lett.* **79**, 4240 (2001).

¹² M. Shatalov, et al., *Appl. Phys. Lett.* **78**, 817 (2001).

¹³ Jianping Zhang, et al., *Appl. Phys. Lett.* **77**, 2668 (2000).

Sample No.	Type	Description	Optical Energy Gap (nm)	CL Peak (nm)	CL FWHM (nm)	Comments
896	Bulk	87% Al (XRD)		238	11.4	
898	Bulk	70% Al (XRD)	245	262	9.6	Brightest band edge emission of all BU samples.
898a	Bulk Faceted	6 mesas (600ux500u)				
898b	Bulk Faceted	4 mesas (600ux500u) 195u average mesa height				
898c	Bulk Faceted	Multiple mesas 925u average mesa height				
1066	Bulk			269	12	
1278	Bulk	72% Al (XRD)	243	274	10.7	First demonstration of stimulated emission at 274nm. 30nm Stokes shift from gap energy
1278a	Bulk Faceted	4x3 mesa array(12total), 600ux500u, 1060u average mesa height				
1281	Bulk	85% (Flux)		243	13	
1283	MQW	Sapphire/AlN(500nm)/10MQWs (Well: 70%AlGaIn 2nm, Barrier: AlN 4nm)		273		CL spectrum same as bulk AlGaIn with same composition as quantum wells. QW effect canceled by Q-confined Stark effect
1285	MQW	Sapphire/70%AlGaIn(~1000nm)/5MQWs (Well: 70% AlGaIn 2nm, Barrier: AlN 4nm)		253		Identical to 1283 but CL blue shifted due to QCF effect less in unstrained QWs
1286	Double MQW	Sapphire/125nm AlN buffer/ 70%AlGaIn(1000nm)/ 20MQWs(Well: 70% AlGaIn 2nm, Barrier: AlN 4nm)/ 20MQWs (Well: 70%AlGaIn 1nm, Barrier: AlN 4nm)		243	18	
1286a	Double MQW Faceted	5x4 mesa array (20 total), 600ux500u				Sample not etched yet due to lack of material for etch rate calibration of layered composition material.
1289	Double MQW	Sapphire/85%AlGaIn(~1000nm)/ 20MQWs (Well:85%AlGaIn 2nm, Barrier: AlN 4nm)/ 20MQWs (Well:85% AlGaIn 1nm, Barrier: AlN 4nm)				
1303	No1GRIN-SCH-DH	Sapphire/ 200nm AlGaIn, 55%Al mole fraction		275		
1304	No2GRIN SCH-MQW	Sapphire/AlN to 67%Al Mole fr AlGaIn grade 50MQWs, 2nm well, 4nm barrier		248		

Bulk $\text{Al}_x\text{Ga}_{1-x}\text{N}$ Materials

During the first half of this Phase I SBIR we have focused on growing and characterizing bulk AlGa_xN films for deep UV emission. The composition of the films was determined by XRD and the optical properties were determined by transmission measurements and cathodoluminescence measurements.

The investigated samples and summary of their properties are listed in Table II.

Table II

Sample Number	Al-Content (Flux measurements)	Al-Content (XRD)	Optical Energy Gap (nm)	CL Peak (nm)	CL FWHM (nm)
1066				269	12
898		70%	245	261.4	9.6
1278	70%	72%	243.5	274	10.7
1281	85%			243	13
896		87%		238	11.4

Bulk samples 896, 898, and 1066 were grown and characterized prior to 1278 and 1281. CL spectra of these first three bulk $\text{Al}_x\text{Ga}_{1-x}\text{N}$ samples having differing Al/Ga ratios were measured at Astralux and are shown in Figure 4. The Astralux CL cold-stage has a 3/4" diameter, allowing multiple samples to be mounted simultaneously for comparisons of relative CL intensity. The electron energy, beam current and focusing, and spectrometer slit widths were the same for all samples. In these spectra, sample 898 shows the greatest band-edge emission intensity and was thus identified as the most promising candidate of these first samples for processing of facets, as described in further detail below.

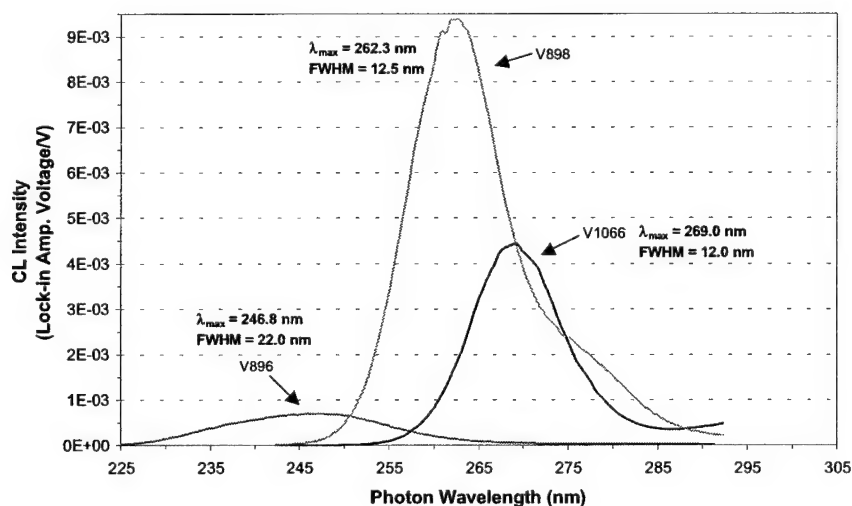


Figure 4. Comparison of relative CL intensities at room temperature for three bulk $\text{Al}_x\text{Ga}_{1-x}\text{N}$ samples.

The composition of the films by XRD was determined from the position of the (0002) diffraction peak. An example of such XRD data is shown in Fig 5.

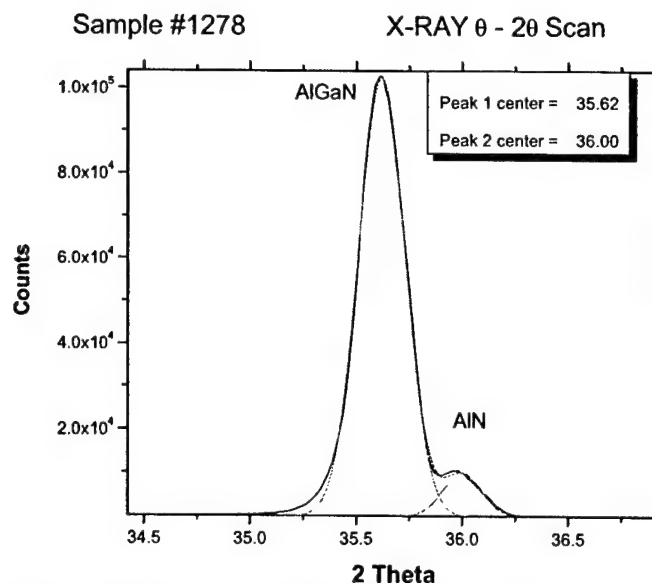


Figure 5. On-axis XRD data of AlGaIn sample 1278. The peak position at 35.62 corresponds to 72% AlN mole fraction.

The optical absorption constant of the same film described in Fig. 4 was determined by transmission measurements.

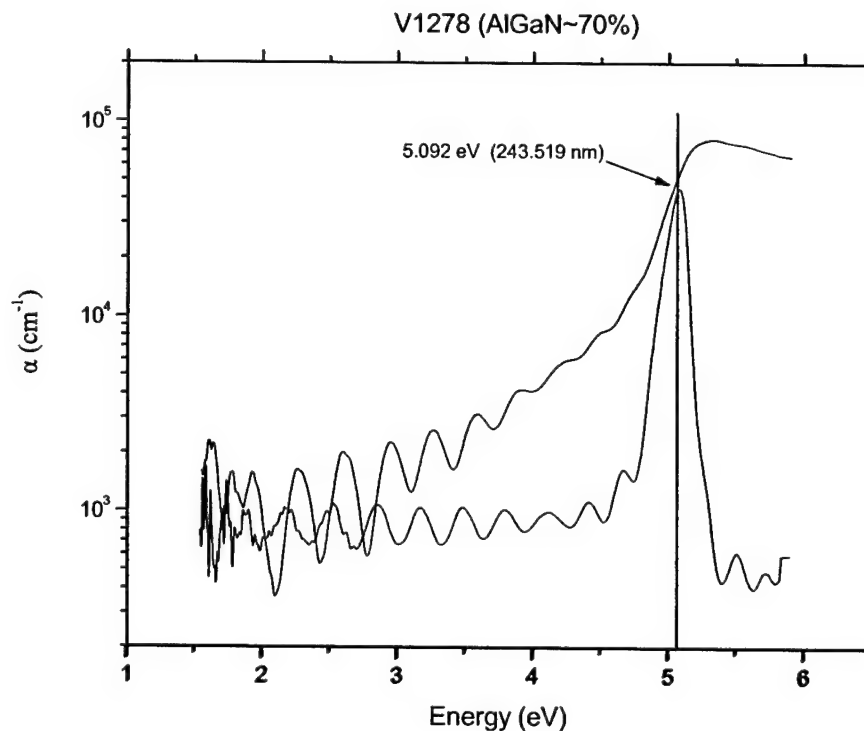


Figure 6: Optical Absorption constant vs. photon energy for sample 1278. Shown below the optical absorption is the derivative of the optical absorption constants with respect to energy. The peak of this the curve determines the optical energy gap as described in the text.

The determination of the energy-gap from the optical absorption measurements is not straightforward. The absorption coefficient of a direct band gap semiconductor above the energy gap α_{par} has a parabolic dependence on photon energy $h\nu$ [Pankove, 1975]:

$$\alpha(h\nu) = A \cdot (h\nu - E_{Gap})^{1/2} \quad (\text{Eq.1})$$

while the absorption below the energy gap has an exponential dependence known as the Urbach edge:

$$\alpha(h\nu) = B \cdot \exp\left(\frac{h\nu - E_0}{U}\right) \quad (\text{Eq.2})$$

where U is the Urbach energy parameter.

The derivatives of Eq. (1) and Eq. (2) are

$$\frac{d\alpha}{dE} \propto \frac{1}{\sqrt{E - E_{Gap}}} \quad (\text{Eq.3})$$

$$\frac{d\alpha}{dE} \propto \exp\left(\frac{E - E_0}{U}\right) \quad (\text{Eq.4})$$

The plot of the derivatives leads to a curve with a sharp peak as indicated in Fig. 6 and the position of the peak determines the energy gap of the semiconductor. A representative CL spectrum is shown in Fig (7)

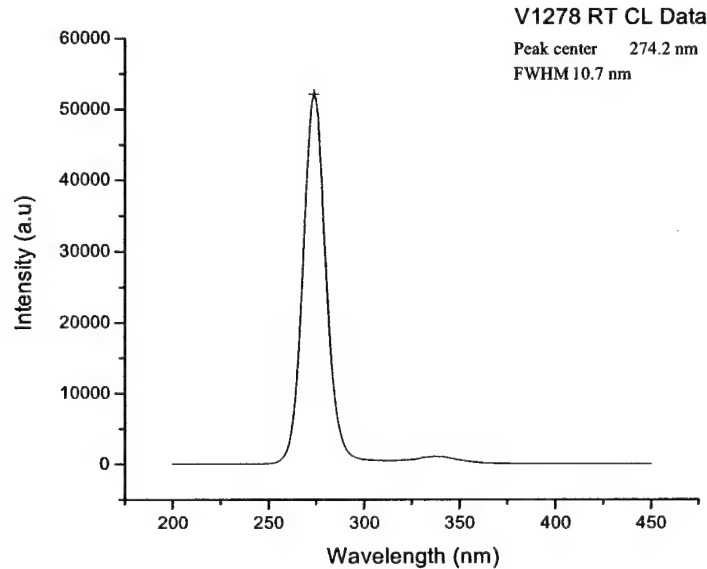
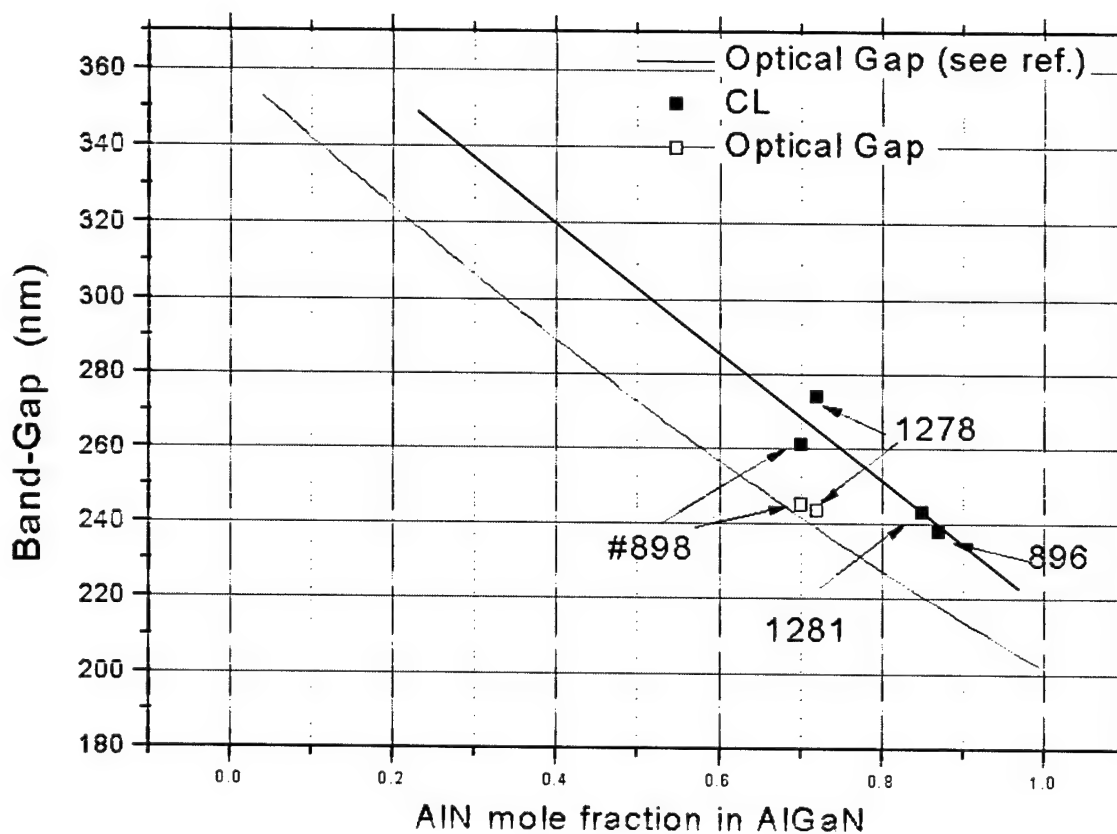


Figure 7: CL spectra for sample discussed in Figs 4 and 5

The optical properties of these AlGaIn films were compared with the existing literature in Fig 8. While our optical energy-gaps determined by the derivative method agree fairly well with optical gaps reported in the literature, the peaks of the CL spectra are red-shifted by 20-30nm with respect to the corresponding optical gaps. The origin of this red-shift (Stokes shift) is potentially due to band-tails due to compositional inhomogeneities arising from partial long-range atomic ordering and phase-separation. An alternative interpretation of the red-shift is that the luminescence peaks are donor-bound excitons. The donor states become deeper with the Al content.



Band parameter data taken from JAP 89,11,5815; June 2001

Figure 8. The solid line is the optical gap reported in the literature in the reference stated. The open squares are optical gaps for samples 898 and 1278 determined in our laboratory by the derivative method described in Fig 5. The solid squares are the peak energies of the CL spectra of the various investigated samples.

Due to the red-shift of the CL spectra it appears that it will be difficult to obtain an CL emission from a **bulk** AlGaIn film at 225 nm. There is a report in the literature (14) [RIKEN] where they demonstrated Photoluminescence measurements at 77K at 220 nm with Al content of 95%. However at room temperature the PL peak should be red-

shifted because the gap becomes smaller at higher temperatures. In a MQW it appears more feasible to obtain emission near 225nm.

MQW Structures

MQW Samples 1286 and 1289 from BU had the shortest wavelength emission peaks of the MQW samples grown during the Phase I program and a comparison of their CL spectra is shown in Figure 9. The achievement of 222 nm emission from sample #1289 is remarkable and demonstrates the great potential of $\text{Al}_x\text{Ga}_{1-x}\text{N}$ MQW structures for electron-pumped deep UV optical sources, which would not suffer from the usual problems relating to p-doping and ohmic contacts for pn junction-based devices. From these spectra, we decided to include sample 1286, rather than 1289, in the first round of facet processing due to the greater emission intensity of this sample. During the Phase II effort, work will continue to grow optimized structures having high emission intensity at the shortest wavelength possible.

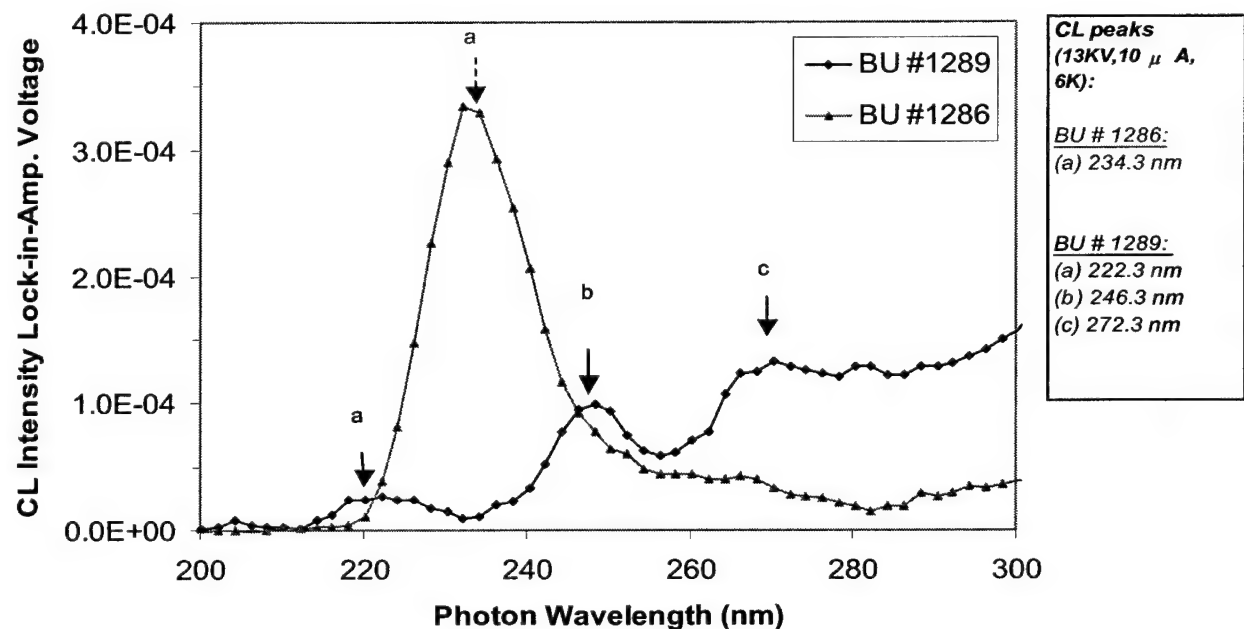


Figure 9. Deep UV emission from two MQW structures grown in the Phase I.

The luminescence spectrum shown below in Fig. 10 for sample 1283 is almost identical with that of a bulk AlGa_N film having the same composition as the quantum wells. We attribute this to the fact that the quantum well effect has been neutralized by the red-shift due to the quantum-confined Stark effect, as described above. For sample 1285 the CL peak is blue-shifted by 20nm with respect to the previous sample although the MQWs were identical. We attribute this to the fact that the quantum-confined Stark effect must be less when the wells are unstrained. For sample 1286 we used the same cladding layer as the second sample and the spectrum is dominated by the twenty,

1nm, MQWs which are on the top of the sample. The CL peak for this sample is at 243nm. These MQWs were studied with 5kV energy in order to absorb the electron beam only in the QWs rather than the cladding and the buffer layers underneath. We see a single peak at 243nm from sample 1286 contributed by the MQWs on the top (well width 1nm). The slight asymmetry of this peak is attributed to luminescence from the second set of MQWs in the bottom (well width 2nm). We see no deep defects up to 400nm.

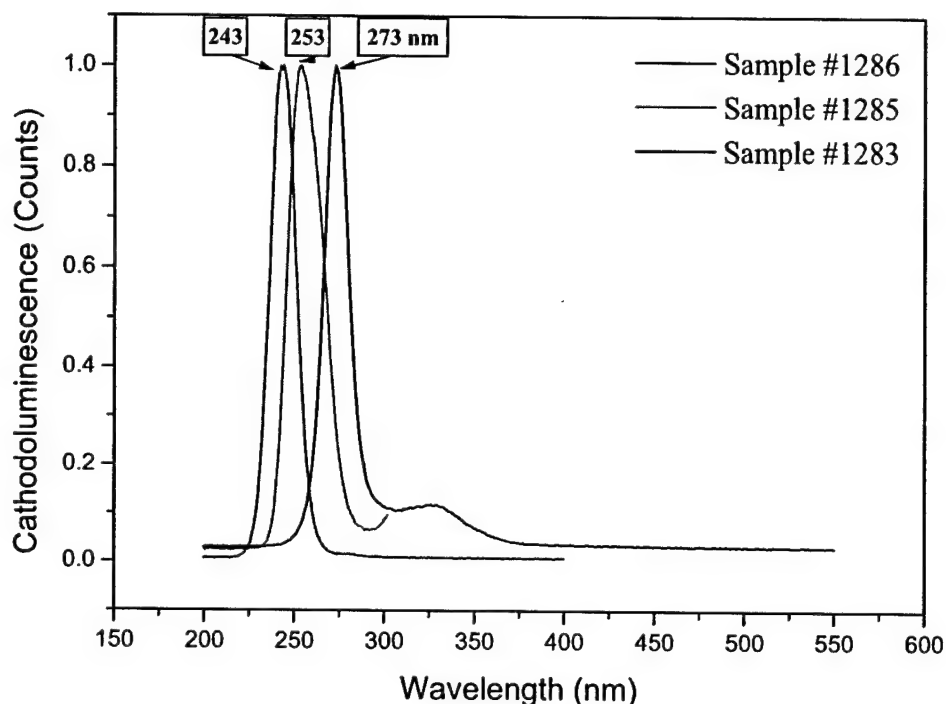


Figure 10. CL spectra of three MQW AlGaIn samples

This data compares favorably with that reported by the RIKEN group in Japan¹⁴. This group reported that a MQW with 1.2nm emits at 229nm at 77K. If we take into account the temperature dependence of the gap that emission should have occurred at 249nm. Thus our data is consistent with the literature. The pumping levels used in our CL measurements are very low, perhaps of the order 50 mA/cm². It seems possible that the electric field inside the quantum wells could be significantly screened by the electrons and holes as the pumping power is increased. This would require a charge density near $\sim 1\text{E}12$ cm⁻² for each well. For example, this might occur if the recombination time were 1E-11 s and the effective pumping rate was $\sim 1\text{E}5$ Wcm⁻². This pumping rate is similar to what may be required for lasing. Possibly then the CL

¹⁴ Hirayama, H., Y. Enomoto, A. Kinoshita, A. Hirata and Y. Aoyagi, "Optical Properties of AlGaIn Quantum Well Structures", JMRs, 11.35, 1999.

wavelength might blue shift if the e-h population is large enough, and that population may be lower than needed to cause lasing. The shift would occur at lower e-h concentration (and also perhaps lower pumping power) for films with lower fields. Such a shift might even predict the imminent onset of lasing.

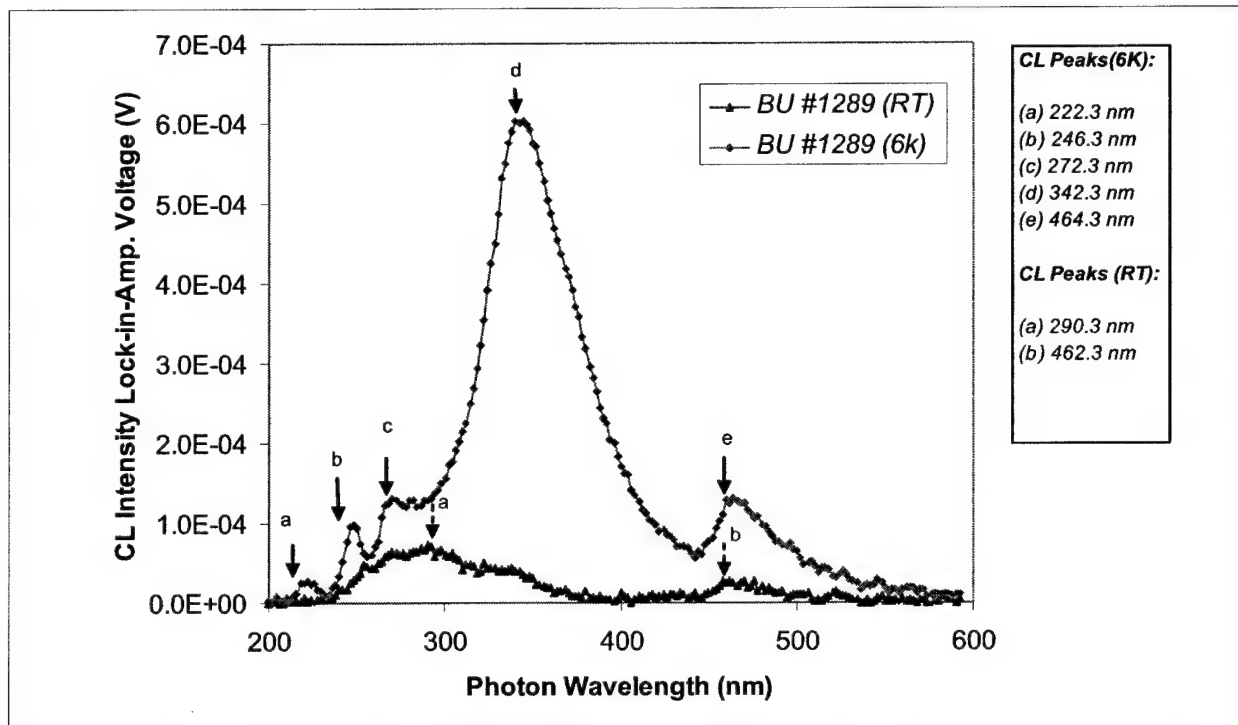


Fig. 11. The CL intensity measured at 13kV with a beam current of 10 μ A at 6K and room temperature for sample 1289.

The sample #1286 in the table, which consists of two sets of MQWs grown on the top of 1 micron thick 72%AlGaIn film, was investigated as a function of probe current. Two MQW stacks were grown: 20 MQWs (72%AlGaIn/AlIn) with well width 2nm and 20 MQWs (72%AlGaIn/AlIn) with well width 1nm. The acceleration voltage in this experiment was 7kV, aimed to excite primarily the MQWs. The peak due to the two sets of MQWs occurs at 240nm and the rather large FWHM is due to the superposition of the spectra from the MQWS with 10A and 20A wells. The second peak 273 nm is due to the CL spectra from the AlGaIn bulk film.

The data in Fig 12 show clearly that the CL intensity of the bulk material increased by a factor of 40 as the probe current varied from 5×10^{-9} A to 1×10^{-7} A, while the CL intensity of the MQWs increased by only a factor of 6. The fact that the bulk CL increases faster than the MQW CL may be due to materials properties and the presence of internal electric fields in the MQW structures. However, we do not have a good understanding of these results at this time. We can only speculate that the problem lies with the excitation mechanism with the two sets of the MQWs each of which is 1000A thick. Based on this interpretation we believe that the ESUVOS

structure based on purely MQWs should be grown to have an overall thickness of 5000Å to 1 micron in order to be excited uniformly. An alternative approach is to design the ESUVOS structure in the GRIN-SCH configuration as samples #1303 and #1304. However in such structures are designed to be edge emitters rather than surface emitters.

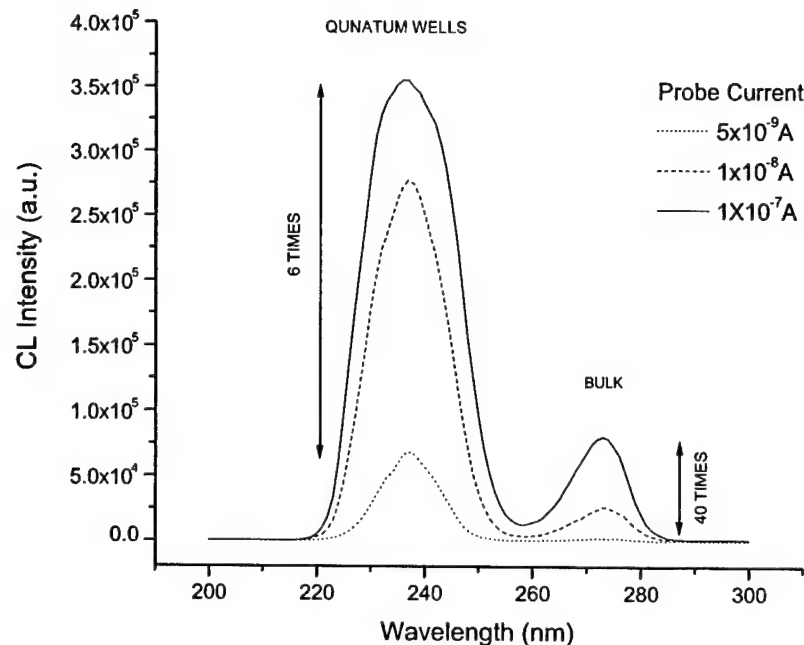


Fig 12. CL spectra of Sample #1286 at different probe currents

GRINSCH Structures

The ultimate proposed III-nitride heterostructure for electron-beam pumping is schematically shown in Fig. 13. Two conditions are necessary for making a compact electron-beam pumped semiconductor laser. First, a low electron current (below 1mA);

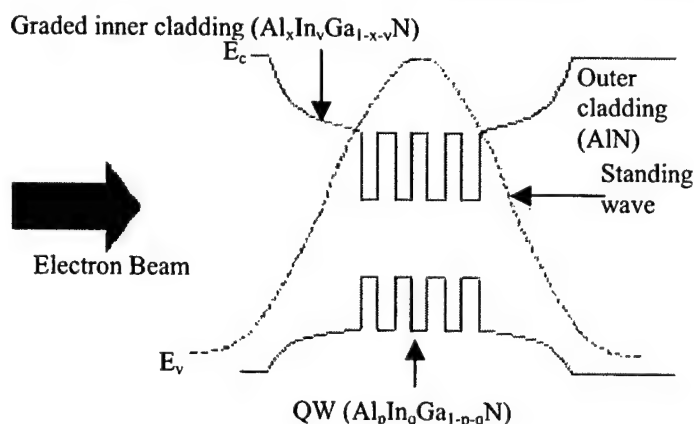


Figure 13. Schematic of the proposed e-beam pumped III-nitride heterostructure.

second, a low accelerating voltage (below 10kV). These requirements are satisfied by a special design of the semiconductor heterostructure. A very low threshold (less than $10\text{kW}/\text{cm}^2$) can be obtained by designing the heterostructure in a MQW-GRINSCH configuration as shown in Fig. 13. However, certain modifications are required to the well-known GRINSCH laser structure in order to be

adapted for electron-beam pumping. With an accelerating voltage less than 10kV the electron-hole pairs are created only near the surface of the semiconductor (approximately 100-500nm). Therefore we will design the laser structure to be asymmetric, with a very thin outer cladding layer on the side of electron pumping. Furthermore, electron hole pairs must be efficiently collected into the MQWs, which constitute the active region of the laser. This function is assured by a graded composition of the inner cladding layer of the heterostructure. The grading will be accomplished by growing the inner cladding layer in the form of digital alloys.

We have completed the growth and characterization at Boston University of two Graded-index separate confinement structures (Samples 1303 and 1304). These structures by design are to be used as edge emitters. Therefore to complete stimulated emission studies we have to etch ridged structures which will be completed at Astralux. In the following we describe the structures grown at BU and their preliminary surface CL results studied at room temperature under 7 KV excitation. We have chosen this excitation energy in order for the electrons to be absorbed in the active region of the device.

Structure 1

The band diagram of structure 1 is shown in Fig 14. The cladding layer was made of AlGaIn, which was graded from pure AlIn down to 67% AlIn mole fraction. The active region consists of a 200 nm of AlGaIn with 55% AlIn mole fraction. The configuration of Fig. 14 was chosen such as to avoid the quantum-confined Stark effect.

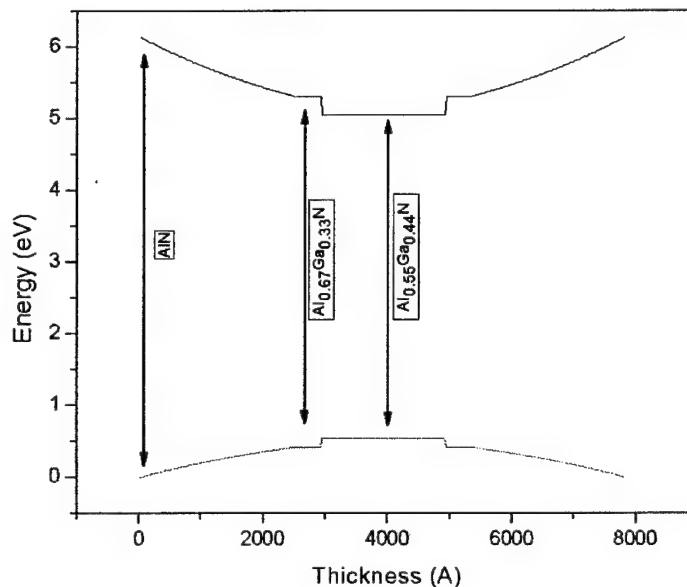


Fig 14: Graded index separate confinement heterostructure (GRIN-SCH) incorporating a double heterostructure as active region.

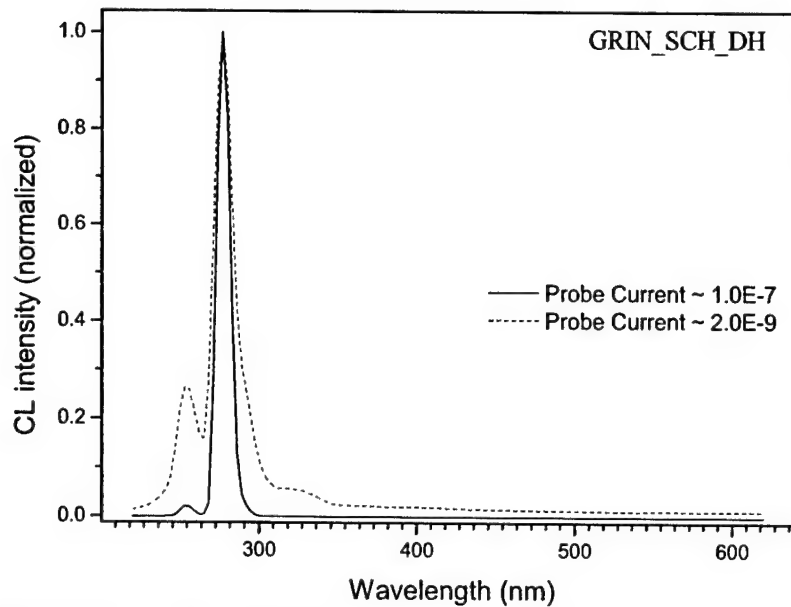


Fig 15: Room temperature surface CL at two probe currents of the structure described in Fig 12.

The surface CL data from structure 1 is shown in Fig 15. There are two peaks in the spectra of Fig 15. The one at 255 nm is attributed to emission from inner cladding layer, which has 67% AlN mole fraction. The second peak at 275 is emission from the heterostructure.

Structure 2

The band diagram of structure 2 is shown in Fig 16. The cladding layer was made of AlGaIn, which was graded from pure AlN down to 67% AlN mole fraction. The active region consists of 50 pairs of AlGaIn/AlN MWQs with nominal well width 2nm and barrier width 4 nm.

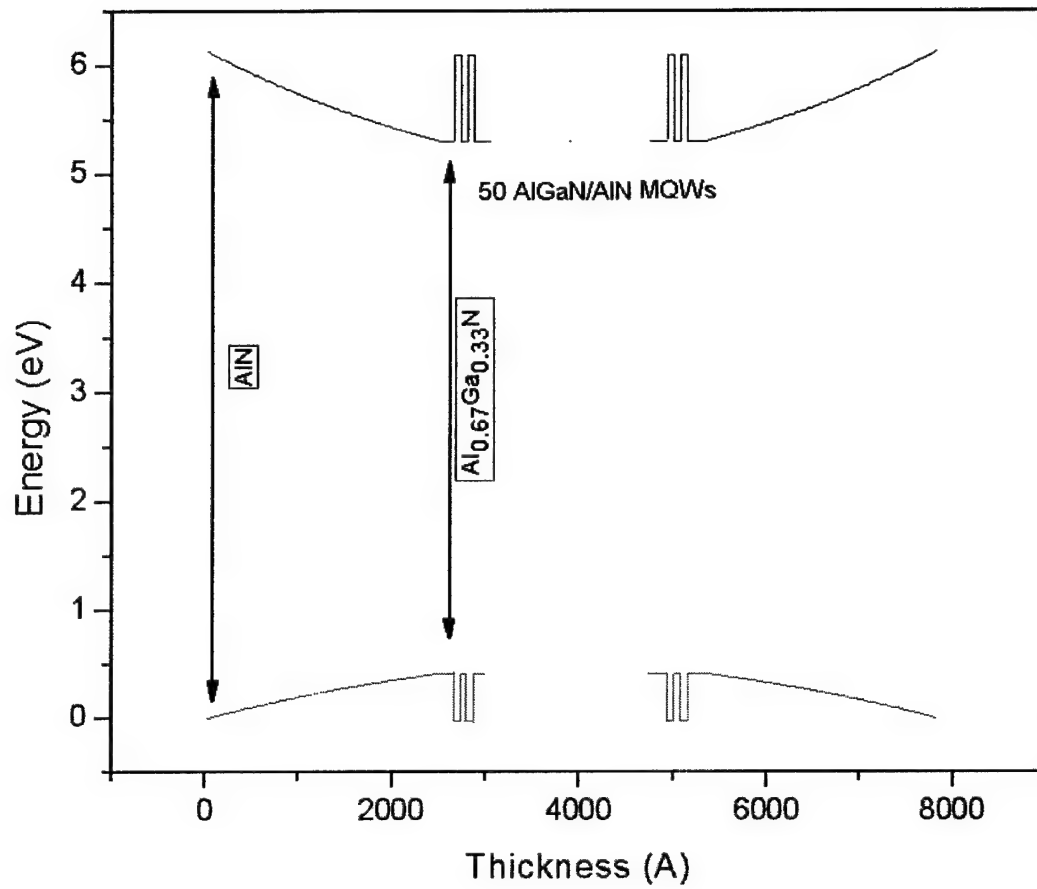


Fig 16. Graded index separate confinement heterostructure incorporating MQWs as active region (GRIN-SCH-MQW).

The surface CL data from structure 2 is shown in Fig 17. The main peak at 248 nm is due to emission from the MQWs. We believe the second peak at about 370 nm is mid-gap emissions from the AlN barriers due to trace amounts of oxygen in the AlN.

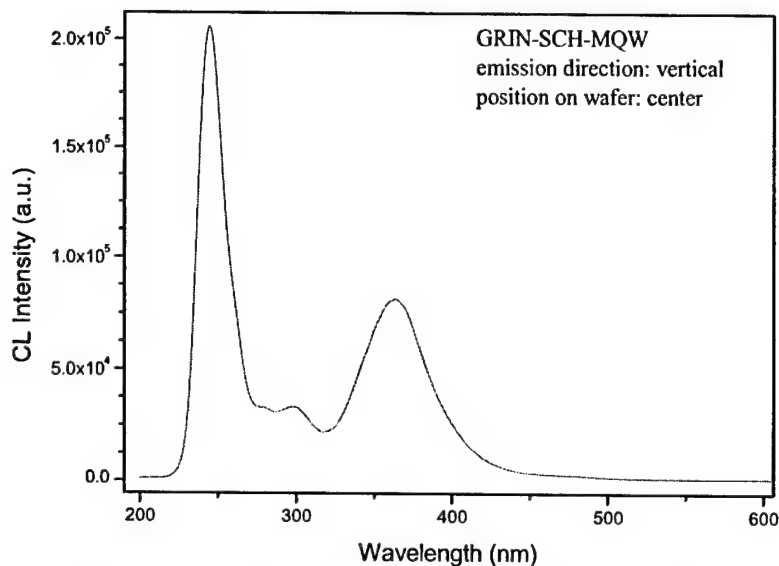


Fig 17: Room temperature surface CL at two probe currents of the structure described in Fig 14.

Note: The compositions stated in structures 1 and 2 will be confirmed by RBS studies. During growth our Flux monitor has failed and we grew the structures based on temperatures of the cells.

Stimulated Emission Results

Initial indications of stimulated emission were observed on sample 1278. Fig 18. below shows the CL spectra measured at 10KV at beam currents from $5.0\text{E-}10$ A to $1.0\text{E-}6$ A. These beam currents were provided by the manufacturer for 30KV excitation. Since we excited the sample at 10KV, the currents probably are smaller. To fit all the spectra in the same figure we normalized the data.

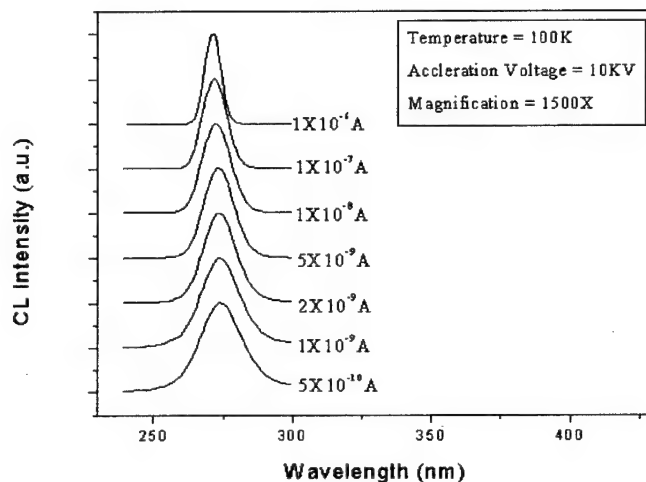


Fig 18: CL spectra of sample BU-1278 measured at 100K at different beam currents

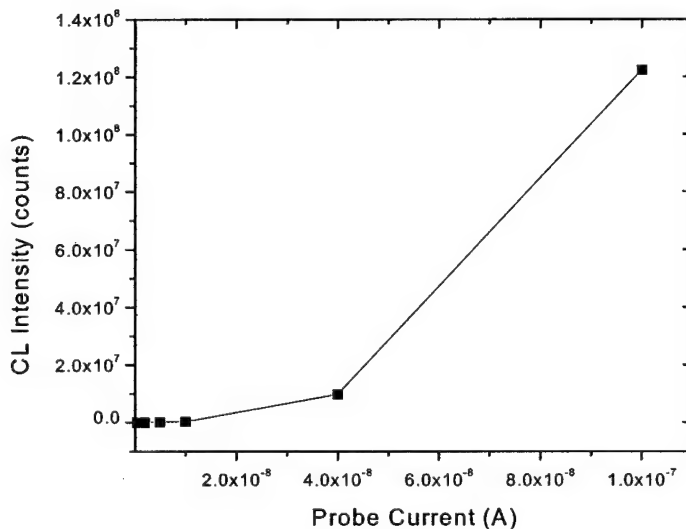


Fig 19: CL Intensity vs. probe current

Fig 19 above shows the CL intensity vs. beam current. The non-linear behavior at higher excitation is evidence of the beginning of stimulated emission.

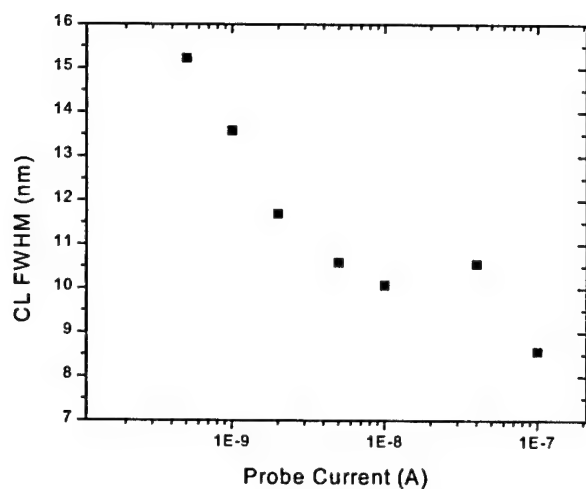


Fig 20: CL FWHM vs. probe current

Fig 20. Shows the CL FWHM as function of beam current. Again, the narrowing as a function of excitation is evidence of beginning of stimulated emission.

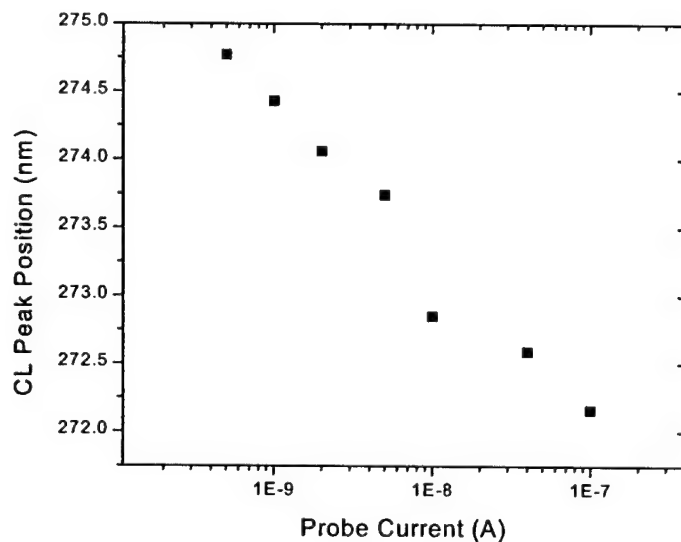


Fig 21: CL Peak position vs. probe current

Fig. 21. above shows the CL peak position as a function of beam current. Again the observed blue-shift is consistent with band-filling.

The stimulated emission measurements were done in an Oxford MONOCL CL system attached to a JEOL SEM instrument. Excitation and collection of the emitted light in this system is described in Fig 22.

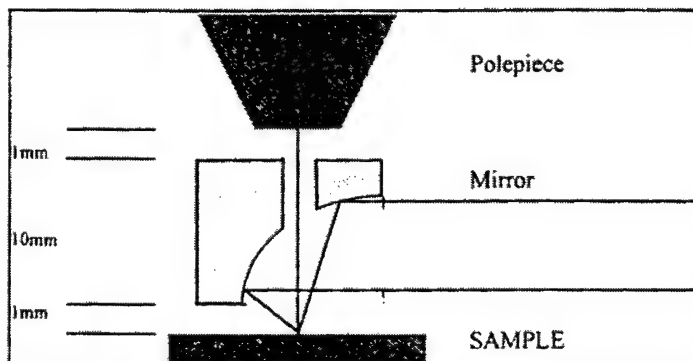


Fig 22: Schematic of excitation and collection of the emitted light of the Oxford MONOCL system

Thus, this system is suitable in measuring the surface CL emission. The system cannot be used to characterize edge emission from mesas. An important issue is how to normalize the data with respect to the beam area. Fig 23 indicates of how the incident electrons diffuse through the material. This diffusion (scattering) process is material dependent and can be calculated by Monte-Carlo simulations. The diameter of the electron beam at entry into the AlGaIn structure is about 1 micron in diameter.

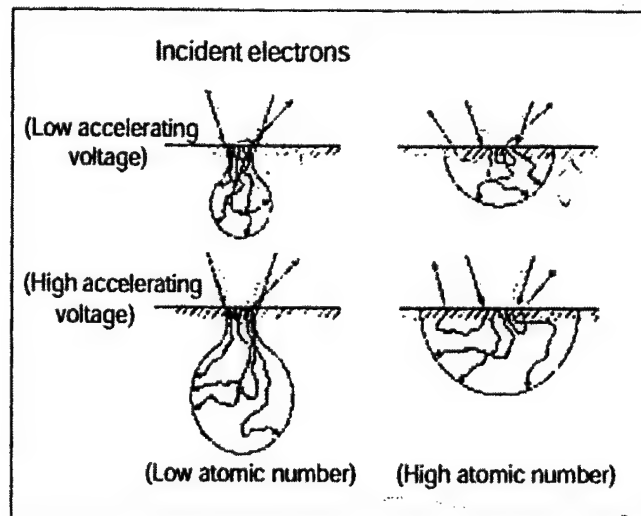


Fig 23: Diffusion of incident electrons for different acceleration voltages (after Ducumb and Shields)

The First stimulated emission data were per observed on a bulk AlGaIn sample (Sample #1278) and reported in the interim report. In summary we have shown non-linear increase in CL intensity by 5 orders of magnitude as the probe current varied from 5×10^{-10} A to 1×10^{-7} . This is shown below in Figure 24. Furthermore the spectral line narrowed from 16 nm to 8 nm as shown in Fig.20. And the line blue shifted from 275nm to 272 nm as a function of probe current.

More recently we have studied another piece of the same sample. The dependence of the CL FWHM vs. probe current for that sample is shown in Fig 23.

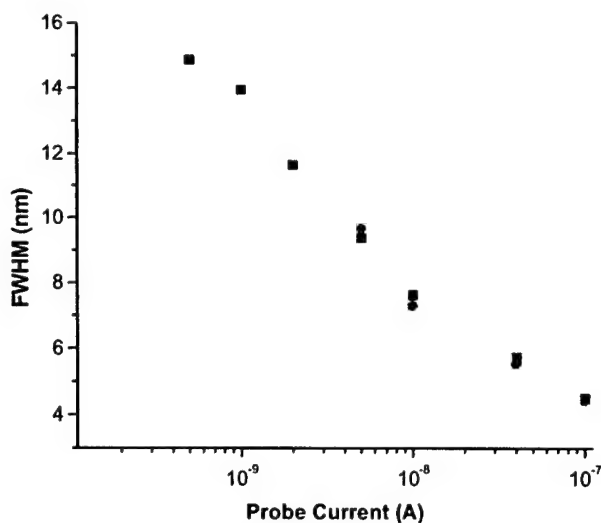


Fig 24. Narrowing of the FWHM of CL spectra with electron beam probe current for Sample # BU-1278 (72%AlGaIn bulk Film) The two colors indicate two different measurement runs on the same sample.

Thus at the highest excitation intensity 10^{-7} A we have obtained a CL spectrum with FWHM of 4 nm. A probe current of 10^{-7} A is the highest current which can be reproducibly used in the BU system and corresponds to an aerial current density about $10\text{A}/\text{cm}^2$. This corresponds to about $50\text{kW}/\text{cm}^2$ of pump power. The CL intensity as a function of probe current is shown in a log-log plot in Fig. 25. This plot clearly shows a five order of magnitude increase in CL intensity for an increase of only two orders of magnitude in pump current.

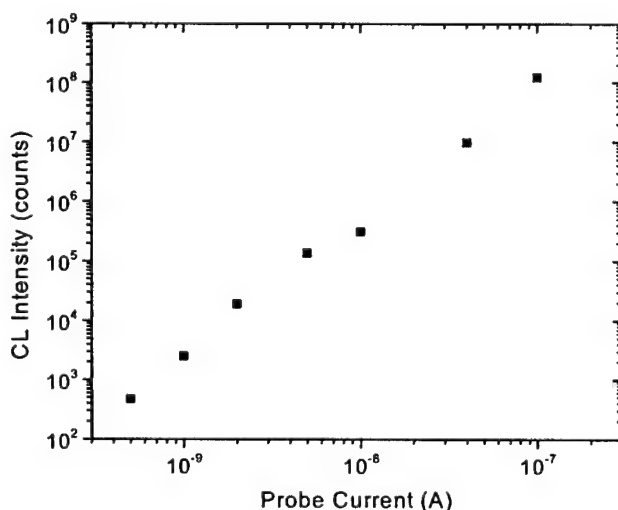


Figure 25. CL intensity versus e-beam current for sample 1278.

Processing of faceted laser dies on $\text{Al}_x\text{Ga}_{1-x}\text{N}$ materials

Preliminary work to produce faceted edge-emitting laser dies from materials grown at BU was undertaken at Astralux during the Phase I program and consisted efforts in the following areas:

- 1) Stripe/mesa photomask design and fabrication
- 2) Stripe/mesa photolithography and facet etch
- 3) Preliminary characterization of faceted samples

During the Phase II program, the work above will continue with the results from the Phase I and early Phase II samples providing feedback on both the optimal materials and modifications to processing techniques. Details of what was done in each area are given below.

During Phase I, the first samples from BU (high Al-content bulk $\text{Al}_x\text{Ga}_{1-x}\text{N}$) were processed to produce faceted samples. However, the CL experimental setups at both BU and Astralux were not designed for detection of edge emission and there was not enough time remaining in the Phase I for the necessary modifications. During the Phase II program these modifications will be made to the Astralux setup to allow the detection of edge emission from faceted samples. Then complete optical characterization will be carried out to refine the ESUVOS laser design. During the Phase II program, the work above will continue with the results from the Phase I and early Phase II samples providing feedback on both the optimal materials and modifications to processing techniques.

Stripe/mesa photomask design and fabrication

A photomask having mesas and stripes of various dimensions was designed and fabricated during Phase I and the layout is shown in Figure 25. The mask structures and mesa/stripe dimensions are detailed in Table III. The stripe sets of differing sizes will be used to measure the gain coefficient and investigate the effect of stripe dimensions on the CL spectrum. The Phase I prototype mesas are 600 microns wide (intended output edge) by 500 microns long (intended optical axis) on a 1.5 mm square die. These dimensions were decided upon for an initial prototype after modeling of the possible electron beam shaping and considering the uncertainty in beam steering for the miniature electron gun in the vacuum package. The excitation length for the ESUVOS laser can be defined with the use of an elliptical electron pump beam, with stripe lithography, or a combination of both. The intent for this initial prototype is to use an elliptical electron beam spot of $\sim 40 \times 100$ microns to define the active gain volume on the mesa as shown in Figures 26 (topview) and 27 (sideview). The issue of electron penetration is discussed further below. The mesa is longer in one dimension to allow a bonding pad in the corner, which won't overlap the active area.

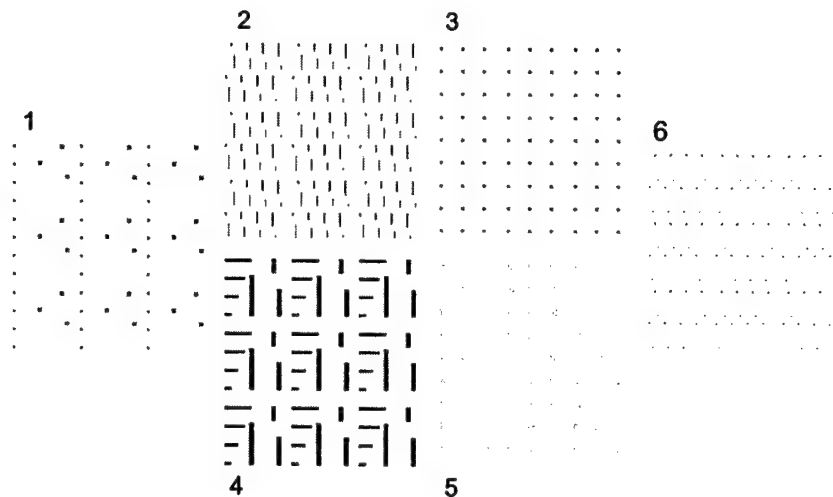


Figure 25. Layout of the ESUVOS mesa/stripe photomask designed and produced during Phase I.

Mask Region	Structures	Structure Dimensions (w x l) in μm	
1	Large stripe set bondpads	200 x 200	300 x 300
2	Small dimensions stripe set	50 x 200 50 x 500 50 x 750 50 x 1000	100 x 200 100 x 500 100 x 750 100 x 1000
3	Phase I prototype mesa bondpads	200 x 200	
4	Large dimensions stripe set	200 x 500 200 x 1000 200 x 1500 200 x 2000	300 x 1000 300 x 2000 300 x 3000
5	Phase I prototype mesas	600 x 500	
6	Small stripe set bondpads	50 x 50	100 x 100

Table III. Structures on the Phase I ESUVOS mesa/stripe photomask.

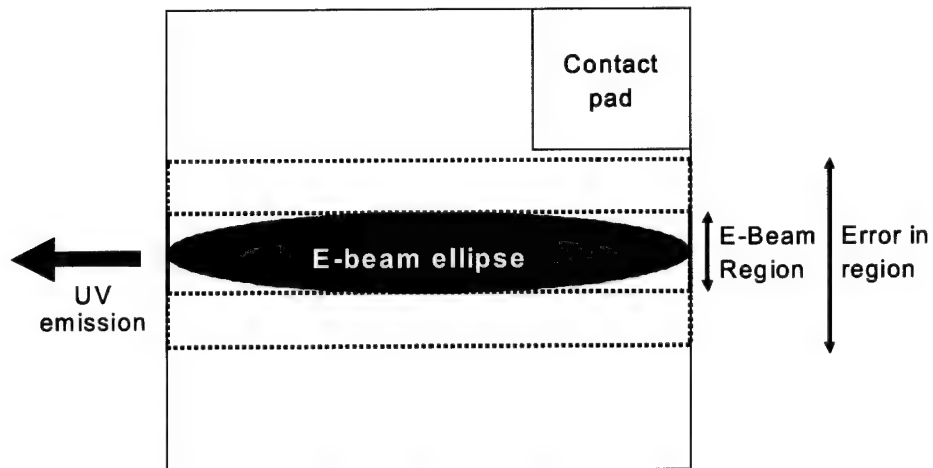


Figure 26. Schematic (topview) of the proposed Phase I prototype mesa showing the elliptical electron beam pump area.

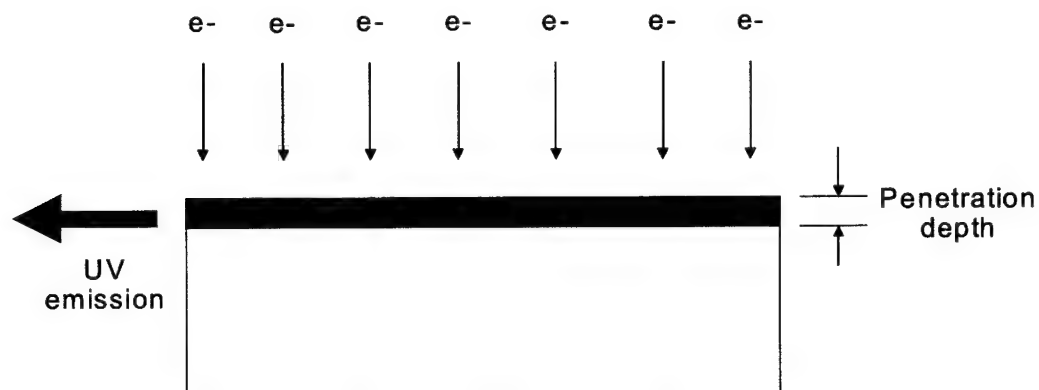


Figure 27. Schematic (sideview) of the proposed Phase I prototype mesa showing the active gain volume formed by the penetration range of the electron beam pump.

Stripe/mesa photolithography and facet etch

For the initial round of facet processing, three samples were chosen out of the 11 wafers grown for the project. Sample #898 was chosen because it had the highest band-edge emission intensity of the first three wafers grown for the project. Sample #1278 was chosen because it gave the stimulated emission results reported above. Finally, sample #1286 was chosen as the best candidate from the MQW samples due to its strong 234 nm emission. The GRINSCH samples were grown late in the Phase I, and therefore could not be included in the first round of facet processing. However, they will be processed in the Phase II program.

Material from the designated samples was diced to appropriate sizes for handling during processing and then spin-coated with AZP4210 photoresist for stripe/mesa lithography. After the samples were patterned, they were etched using Ar/Cl₂ chemically assisted ion beam etching (CAIBE). Figure 28 shows an optical microscope photograph of one of the Phase I prototype mesas etched in sample #898b during Phase I.

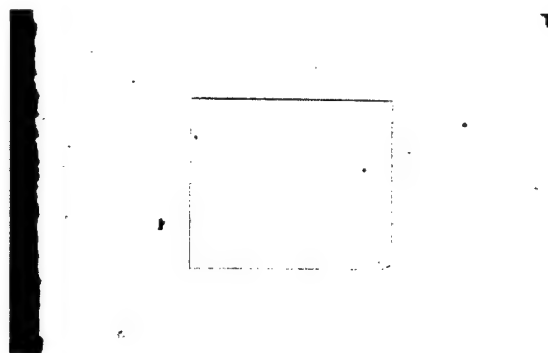


Figure 28. 50X image of a Phase I prototype mesa etched in a bulk sample.

The CAIBE dry etching technique allows for independent physical and chemical etch components via separate control of ion beam power and gas flows. Furthermore, it has been demonstrated that the CAIBE technique provides an anisotropic etch for Al_xGa_{1-x}N, resulting in smooth, near-vertical sidewalls.¹⁵ The CAIBE etch rate calibration for our 70% Al-content bulk materials is shown in Figure 29. The CAIBE etch rate measured for our bulk material is nearly an order of magnitude less than the rate for GaN under the conditions used, which were previously optimized to result in smooth surface morphology. Other groups have also found that the CAIBE etch rate for Al_xGa_{1-x}N is strongly dependent on Al content. However, by adjusting the Cl₂ concentration it should be possible to enhance the rate for our high Al-content films. It was decided to postpone this adjustment until the Phase II program, since some reoptimization of etch parameters will likely be necessary to result in smooth facets. Etching the MQW and GRINSCH samples to a specific depth is a

¹⁵ I. Adesida, C. Youtsey, A.T. Ping, F. Khan, L.T. Romano, and G. Bulman, *MRS Internet J. Nitride Semiconductor Res.*, **4S1**, G1.4 (1999).

difficult matter due to nonuniform layer structure of these samples. In the Phase II program, several practice etch runs on calibration material will be necessary to calibrate the etch to a certain depth.

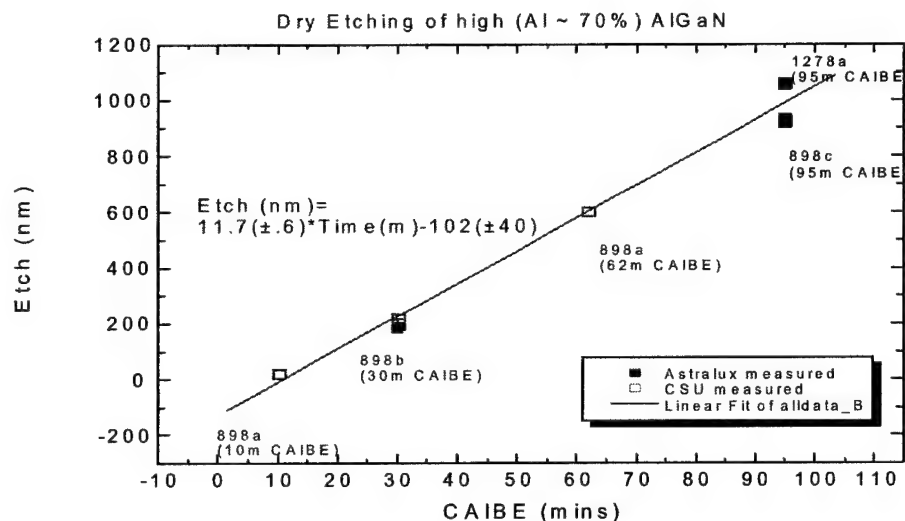


Figure 29. CAIBE etch rate calibration for 70% Al-content Al_xGa_{1-x}N.

The target etch depth should not exceed the thickness of the optically active Al_xGa_{1-x}N layers to ensure that only the active layer(s) rather than the growth buffer layer is exposed along the vertical edge created by the etch. However, it is also important to take into account the pump electron beam penetration range for our ESUVOS device. If the penetration range is less than the thickness of the active layer, it is preferable to etch to a depth equal to the penetration range, in order to minimize the possibility of CAIBE-induced surface damage. The general Kanaya and Okayama expression¹⁶ can be used to estimate the electron penetration range (R_e in μm) for our materials as a function of the electron energy in keV (E_b):

$$R_e = (0.0276A/\rho Z^{0.889})E_b^{1.67} \quad (\text{Eq.5})$$

where ρ is the density in g/cm^3 , and A and Z are the formula-weighted averages of the atomic weight and number of the Al_xGa_{1-x}N material, respectively. For the 70% Al-content bulk Al_xGa_{1-x}N samples from the Phase I project, R_e is approximately 300nm at the 5 keV electron energy that will be used in the initial ESUVOS prototype.

¹⁶ K. Kanaya and S. Okayama, *J. Phys. D.* **5**, 43 (1972).

Preliminary characterization of faceted samples

A Dektak profilometer was used to measure facet heights, stripe profiles, and calibrate etch rate. Table IV shows a summary of the key information for the processed samples.

Sample #	Sample Type	Near-Bandedge Lambda max	Sample Dimensions / Patterned for	Number of Mesas	Average Measured Mesa Height (nm)
1278a	Bulk $\text{Al}_x\text{Ga}_{1-x}\text{N}$ 72% Al	272-275 nm	7.2 mm x 5.7 mm / prototype mesas (600 x 500 microns)	12 (4x3 array)	1060
898b	Bulk $\text{Al}_x\text{Ga}_{1-x}\text{N}$ 70% Al	262 nm	5.1 mm x 4.5 mm / prototype mesas (600 x 500 microns)	4	195
898c	Bulk $\text{Al}_x\text{Ga}_{1-x}\text{N}$ 70% Al	262 nm	10.8 x 6 mm / Small & large mesas of various sizes for gain coefficient measurement	multiple	925
898a	Bulk $\text{Al}_x\text{Ga}_{1-x}\text{N}$ 70% Al	262 nm	5.2 mm x 5.1 mm / prototype mesas (600 x 500 microns)	6	N/A-CAIBE etch rate calibration sample
1286a	$\text{Al}_x\text{Ga}_{1-x}\text{N}$ Double MQW	234-243 nm	7 mm x 8 mm prototype mesas (600 x 500 microns)	20 (5x4 array)	N/A-Sample not etched yet due to difficulty in calibrating etch rate for alternating composition MQW layers & lack of material for calibration.

Table IV. Summary of key parameters for faceted samples produced in Phase I.

Optical microscopy and scanning electron microscopy (SEM) were used to examine edge profiles. Figure 30 shows an SEM image of a mesa etched in a bulk $\text{Al}_x\text{Ga}_{1-x}\text{N}$ sample #898b. The surface morphology shows some damage due to processing and/or cleaning. In Phase II, further SEM studies will be undertaken to understand and minimize the source of this damage.

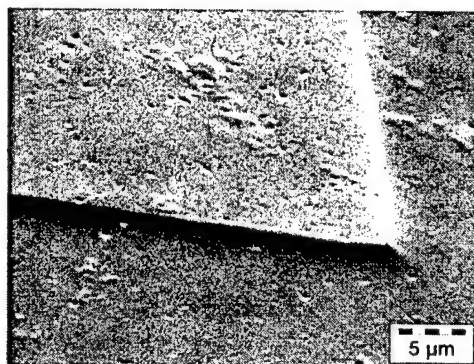


Figure 30. SEM image (6750X, 55° tilt) of a prototype mesa etched during Phase I.

Summary of $\text{Al}_x\text{Ga}_{1-x}\text{N}$ Materials Results

The stimulated emission results shown above agree well with pumping levels required for stimulated emission in pn junction devices. Stimulated emission is commonly believed to occur at pump power levels about $10\text{kW}/\text{cm}^2$ in MQW devices. At 5kV of e-beam pump voltage, this corresponds to $2\text{A}/\text{cm}^2$. Our estimate for stimulated emission from bulk material was about $250\text{kW}/\text{cm}^2$ in the interim report. The results we have demonstrated here show strong stimulated emission at e-beam currents of 10^{-7}A . At an estimated e-beam spots size of 1 micron diameter, this corresponds to about $10\text{A}/\text{cm}^2$ or $100\text{kW}/\text{cm}^2$ at the 10kV e-beam voltages employed. This is well within the range of other investigators. The major surprise from this data is that we achieve such robust stimulated emission in bulk material without mirror facets at a relatively low power density.

Emission linewidth is a major issue for application of semiconductor lasers to Raman spectroscopy. The oscillation bandwidth of the AlGaN emitter is expected to be of the order of 0.5nm when operating as a laser. At a wavelength of 250nm, this corresponds a bandwidth about 80 cm^{-1} . The longitudinal mode spacing of the laser is expected to be between 50GHz and 100GHz (i.e. 1 to 4 cm^{-1}) for devices ranging from 500 μm to 1000 μm in length. Therefore, within the oscillation bandwidth of the device, we expect as many as over 20 longitudinal modes. This bandwidth is too large for use in Raman identification of organisms. However, we have developed a method of limiting the bandwidth to about 20 cm^{-1} with about 5 operating longitudinal modes. This will be discussed in more detail later related to the ability to discriminate biological agents, in Section 3.5.

3.4.3 Electron Source Design

Several changes have occurred in our approach to the electron source for the ESUVOS. We are presently using a diamond microtip array, field emission electron source from Extreme Devices in Austin, TX. Below are illustrations and photographs of this field emission array.

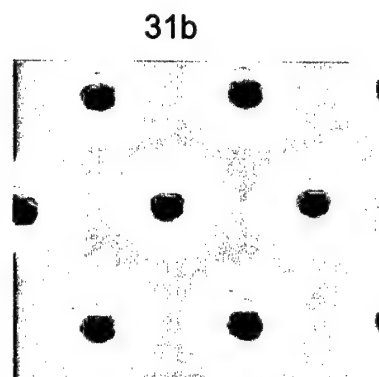
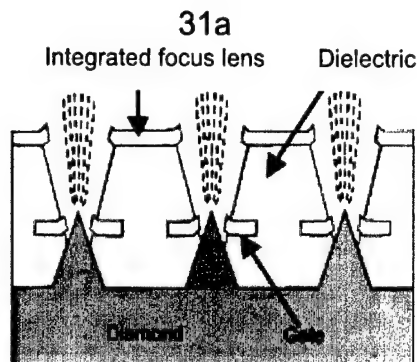


Figure 31 a & b. Diagram(a) and microphotograph(b) of diamond microtip field emission (DMFE) array (courtesy of Extreme Devices, Austin, TX)

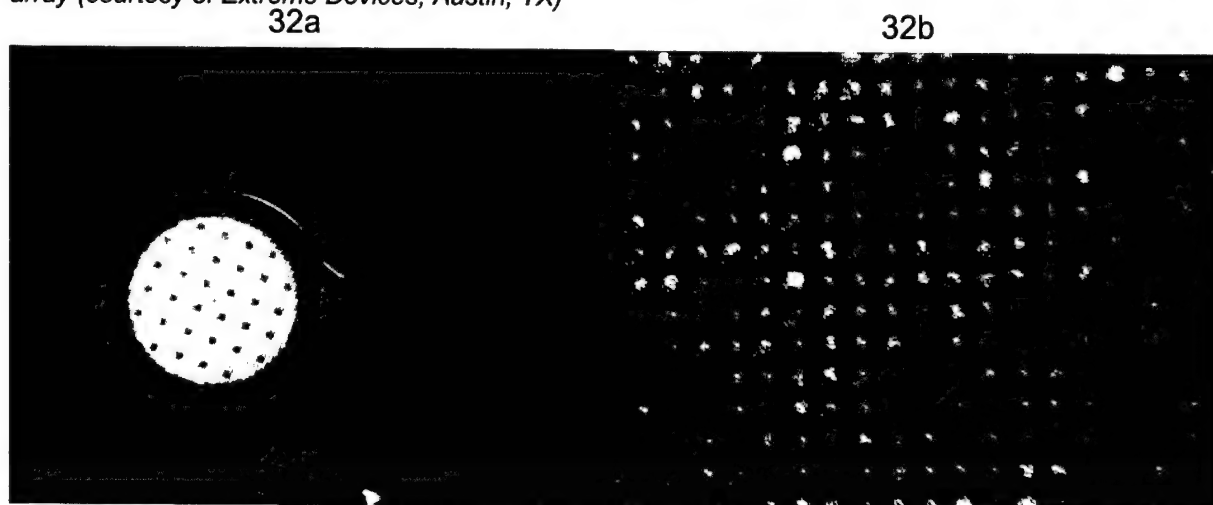


Figure 32a&b. Photos of overall view of diamond microtip array (a) and closeup (b)

The overall diameter of the array above is 250 μm and the pitch spacing between microtips is 5 μm . The array is comprised of approximately 1000 diamond microtips.

The performance of the three DMFE array samples is shown below in Fig. 33. These arrays were identified by wafer number, row number and column number with Series 1 = 3105/26/16; Series 2 = 3105/26/11; and Series 3 = 3105/10/22. Figure 33 demonstrates the ability to achieve about 1mA of emission at an extraction voltage about 300V.

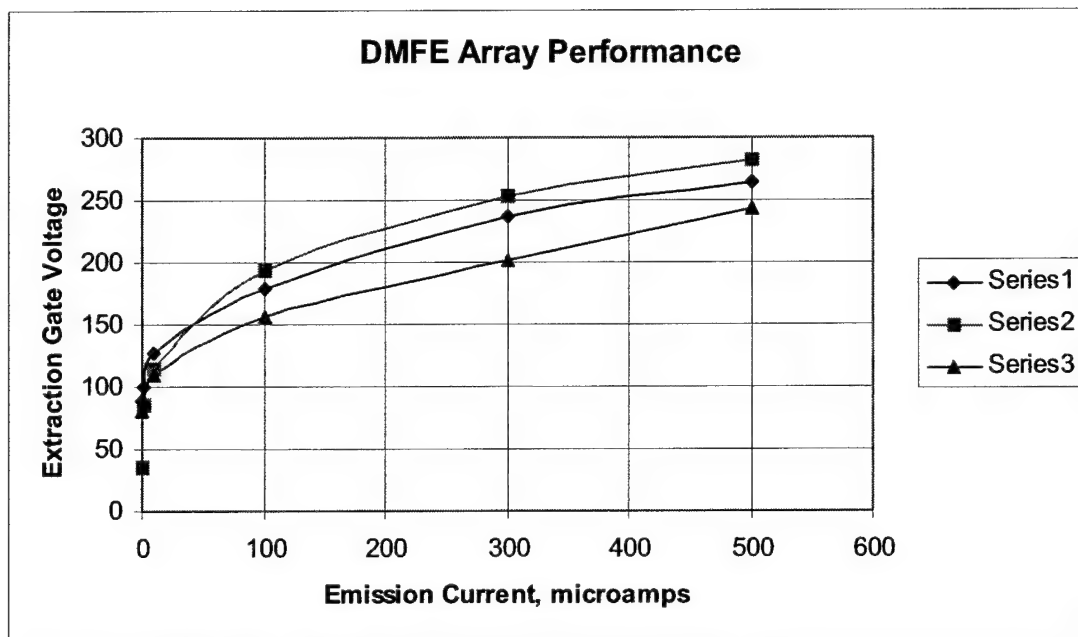


Figure 33. Performance of three diamond microtip field emission arrays

The expected pumping requirements are about 10 μA to 100 μA , focused into an area about 2 μm by 500 μm (1000 μm^2) at an accelerator voltage about 5kV. This corresponds to an e-beam pump power density between 5kW/cm² and 50kW/cm². This is substantially less than the 250kW/cm² originally estimated for stimulated emission from bulk material in the interim report. We believe the evolution of the MQW design will enable reduction of this pumping power density requirement to the 10kW/cm² level, corresponding to a pumping current about 20 μA . Some estimates are that MQWs can reduce the pumping power density by 25X, but we are taking the conservative estimate.

3.4.4 Electrostatic e-beam focusing methods and configuration

Electron emission from the DMFE array will be focused onto the AlGaIn target using an electrostatic lens. The geometry of the electrostatic lens is determined by a solution to Poisson's Equation, $\nabla^2 V = -\rho/\epsilon_0$, where V is the electric potential, ρ is the space charge density, and ϵ_0 is the free space permittivity. Several software programs are available for modeling electron gun designs. These include SIMION, Integrated Engineering Software's Lorentz, and Ansoft's Maxwell 3D.

The proposed electron source is an array of field emission points with a pitch about 5 μm and covering a diameter about 250 μm . At the ALGAN target some 5 mm away, the beam footprint was first estimated to be approximately 40 by 300 μm in order to create the sufficient current density for lasing. This necessitated developing the electrostatic equivalent of a simple cylindrical convex lens in optics.

The lens would thus be required to produce an image reduced to about 16% of the source dimension in the X direction, while enlarging the beam width (Y dimension) by approximately 20%. It was anticipated that a slot type lens would be required.

A number of criteria were thought to be important and were used to evaluate the results of the different lens designs.

- a) Simplicity - if possible a single lens element was most desirable
- b) Efficiency - the lens should intercept the fewest electrons possible.
- c) Focus Quality – maximize the number of electrons landing within the target footprint.
- d) Lens Potential – to minimize insulation issues, lens potential should be close to either target or source potential.
- e) Sensitivity to voltage changes - Make the design as voltage-Insensitive as possible.
- f) Ease of fabrication

The final design was a practical compromise of these considerations.

Electrostatic Lenses

There are two basic types of electrostatic lenses – cylindrical and aperture (also known as the Calbick) lenses. The properties of these and more complex systems are discussed extensively in the classic work "Electrostatic Lenses" by E. Harting and F.H.Read ¹⁷ and in summary form in "Building Scientific Apparatus, by J. H. Moore et al ¹⁸. Beam trajectories were modeled using SIMION v7.0, a 3-D finite difference computer program¹⁹.

Cylindrical lenses are attractively simple, but produce a uniform focusing action and are thus not well suited for the asymmetric imaging require here. They were evaluated at first to provide insight to the requirements and to obtain estimates of beam efficiency that might be achievable. Figure 34 shows electron trajectories modeled for a single cylindrical lens, producing the desired 6 to 1 reduction at the target..

¹⁷ "Electrostatic Lenses", E. Harting and F.H. Read, Elsevier, New York, 1976

¹⁸ "Building Scientific Apparatus", John H. Moore, C. C. Davis, M. A. Coplan and S. C. Greer, Addison Wesley, 1989, 2nd Edition

¹⁹ SIMION 3D Version 7.0, David A. Dahl, Idaho National Engineering and Environmental Laboratory, Idaho Falls, ID.

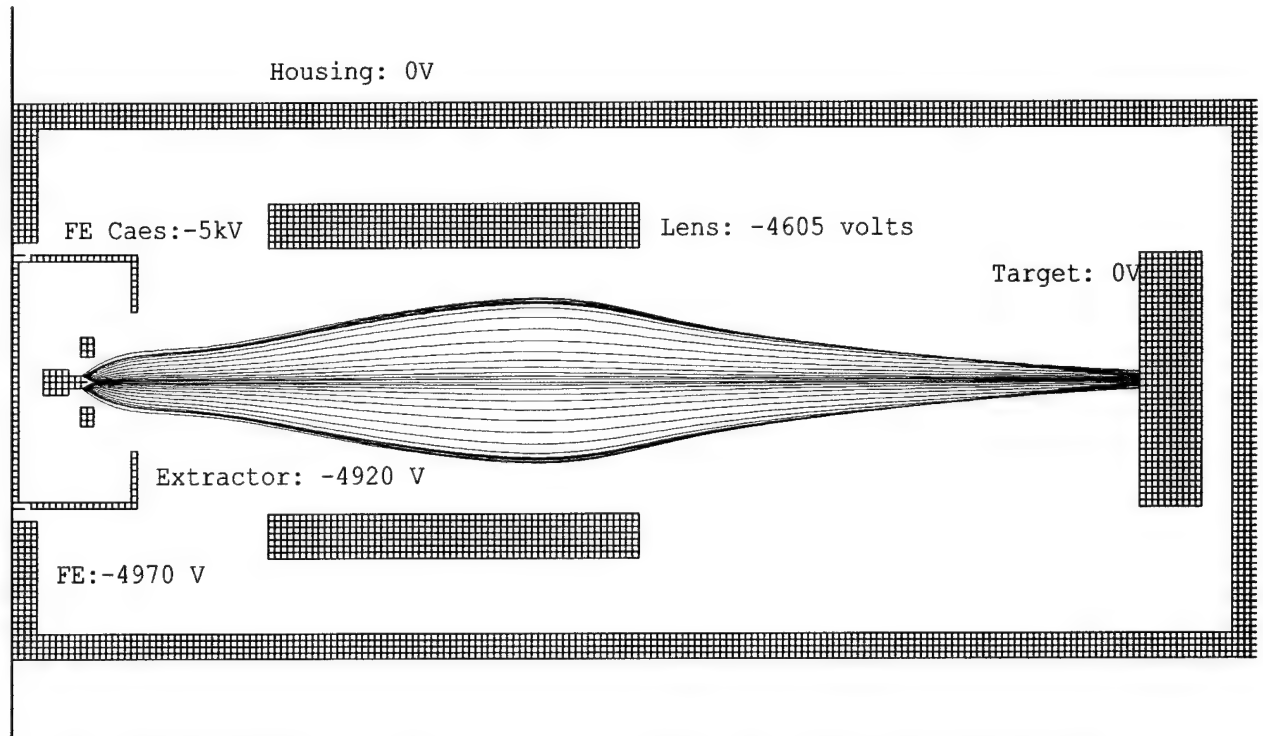


Figure 34. Shown at approximately 40X scale (1 sq = 25 um) , a single lens element focuses beam from DMFE source to about 50 um spot, with voltages as shown. Adjusting lens voltage changes spot size.

Aperture Lenses.

Two types were evaluated – circular aperture and rectangular. The circular aperture lenses were much easier to model, and thus were used to obtain the general positions and voltages for the 3D model of slot lens.

Equations 6 and 77 apply to circular apertures, equations 8 and 9 are for slot lenses (Ref.18).

$$f = 4V/(E_B - E_A) \quad \text{Eq. 6}$$

where E_A and E_B are the fields in front and behind the lens aperture, as given by equation 7.:

$$E_A = (V_{\text{Lens}} - V_{\text{source}}) / D_{\text{source to lens}} \quad \text{Eq. 7}$$

$$E_B = (V_{\text{Target}} - V_{\text{Lens}}) / D_{\text{Target to Lens}}$$

where the V's stand for the respective voltages.

For the slot lens, where the x dimension is $\ll y$.

$$f_x = 2V_{\text{lens}} / (E_B - E_A) \quad \text{Eq. 8}$$

$$f_y = \infty \quad \text{Eq. 9}$$

Notice that equation 8 predicts a slot lens has half the focal length (i.e.: is stronger) of the circular aperture lens. The uniform fields E_A and E_B are approximately obtained in the ESUVOS device described here.

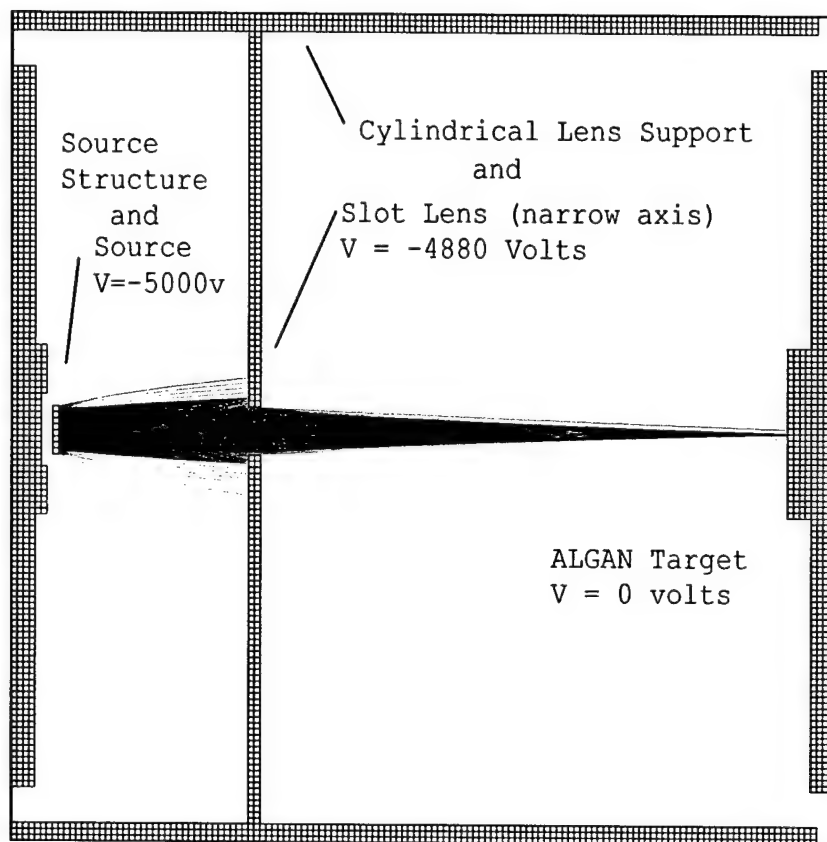


Figure 35. A 2D axially symmetric or cylindrical model of the ESUVOS device producing a 40 μm focus. For modeling simplicity, the narrow axis of a slot lens has been represented by a circular aperture in cross-section. The circular symmetry creates optimal focus at somewhat different voltages from the slot lens, modeled in Figure 36.

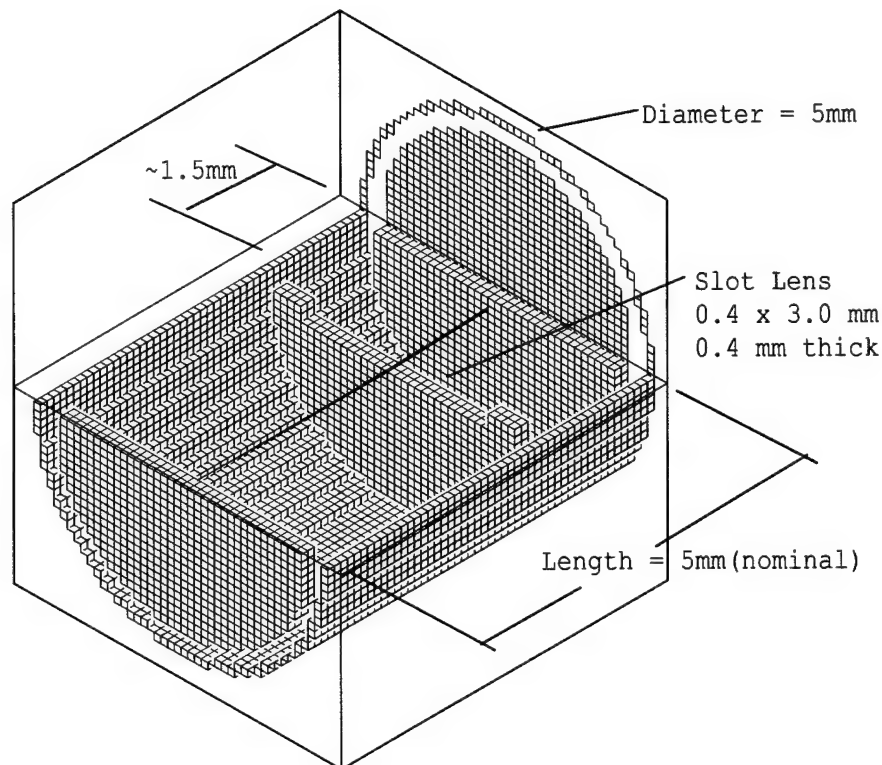


Figure 36. Cut-away 3D view of the ESUVOS model with a true slot lens. The source is at -5000 volts, while the slot lens is optimized for focus at -4720 volts, 280 volts positive relative to the FE source. The lens achieves a magnification of approximately 0.16 in the Y direction and 1.1-1.2 in the X direction. This concentrates the electron beam into a footprint of about 40 by 300 microns on the ALGAN target.

Recent data has suggested that beam current densities may need to be higher for optimal laser drive. The narrower e-beam footprint is obtained by changing the lens voltage. But because of the lens aberration, the lens position may also have to be shifted to keep the beam throughput efficiency high. Analysis of this continues.

3.4.5 ESUVOS Packaging

The device design direction we are presently pursuing is not the most compact configuration possible. However, we believe it will be relatively easy to fabricate since it is an open frame design similar to a traditional butterfly pack used in the opto-electronics industry. The overall, finished device, view is shown below in Fig. 37. The laser beam is emitted from the side of the package through a brazed in sapphire window. Sapphire has the same thermal expansion coefficient as Kovar and provides an excellent hermetic seal.

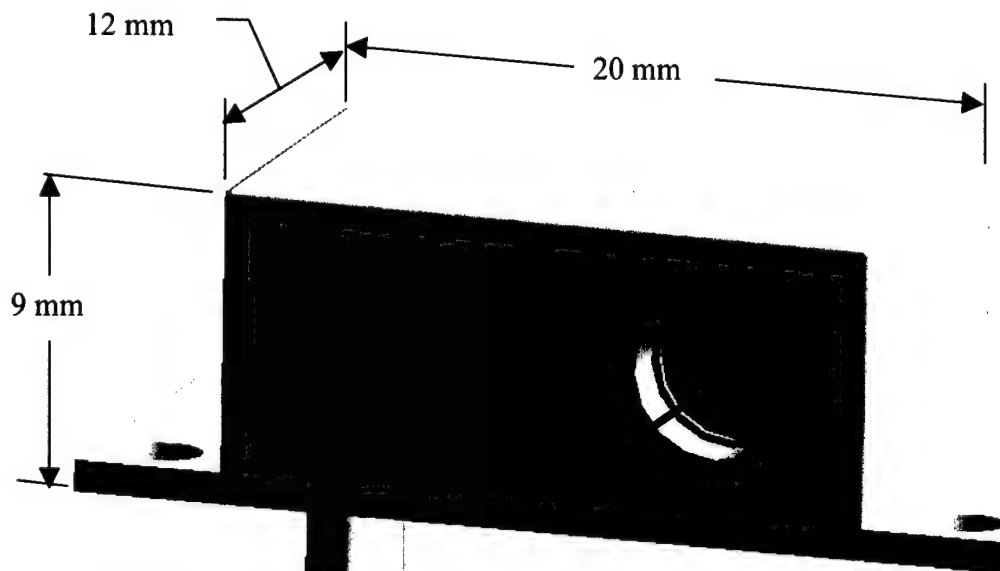


Figure 37. Illustration of overall ESUVOS

Below in Fig. 38 is an illustration of the internal assembly of the device with the copper substrate for the AlGaIn die, electrostatic focusing lens, diamond microtip field emission array electron source and voltage divider resistors.

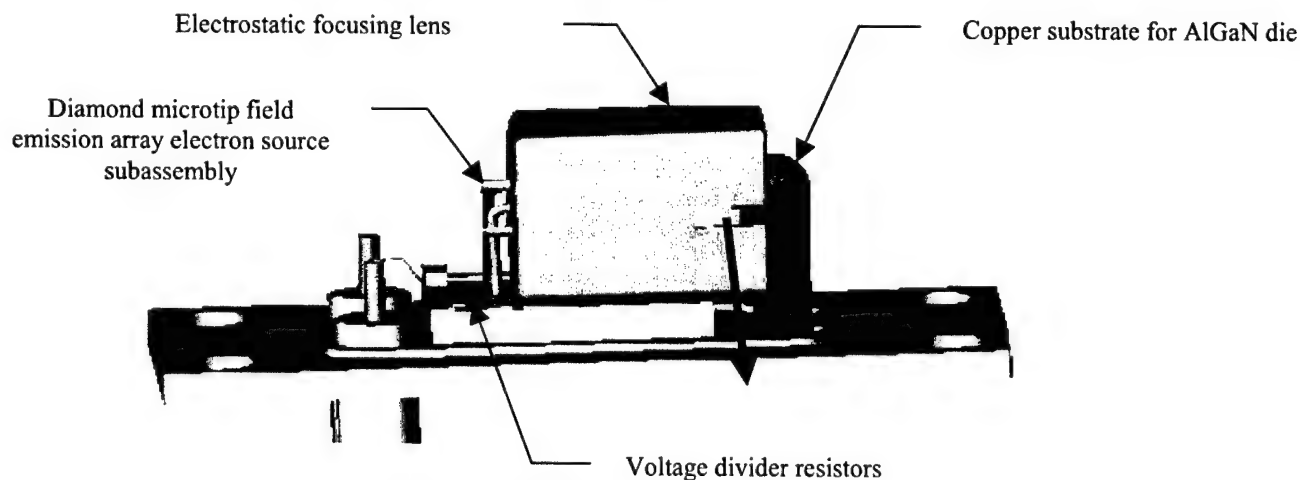


Figure 38. Internal components of ESUVOS

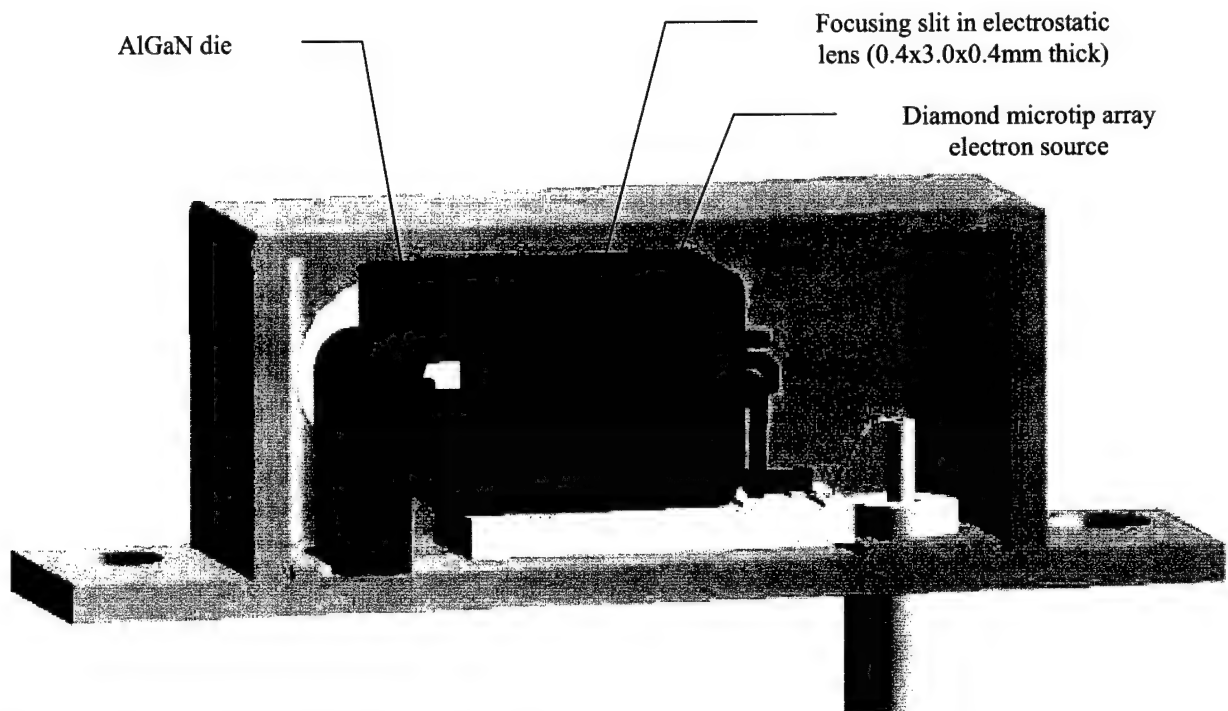


Figure 39. Cross-section illustration of ESUVOS

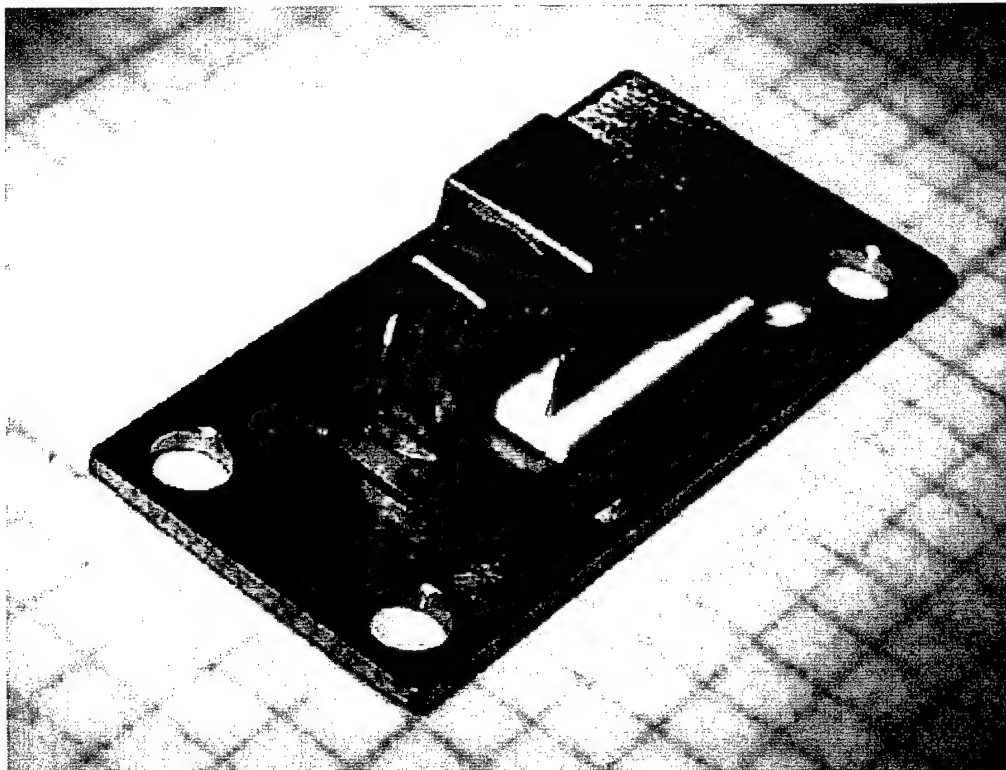


Figure 40. Photo of ESUVOS base assembly

AlGaIn sample mounting

Assuming what we believe to be the worst case pumping power requirements, the temperature rise of the AlGaIn chip resulting from this pumping is estimated from Planck's law to be 324°K with 10W of e-beam pumping and 182°K with 1 W of e-beam pumping. This assumes an overall radiation emitter area about 1mm² and no conduction cooling. These temperatures are not expected to be problematic for the sample materials from a damage point of view. However, the issue of thermal quenching of the exciton is yet to be established. However, we also believe we can provide substantial conduction cooling without impairing the simplicity of the device which would significantly reduce chip operating temperatures.

Vacuum package configuration and process issues

The major vacuum packaging and processing issues include: vacuum outgassing and high voltage free space and surface breakdown issues. The design goals for the device are to make it as miniature as possible. This necessarily means the device will have a large surface to volume ratio compared to larger vacuum devices, which could lead to outgassing issues. Materials and processing methods to minimize vacuum outgassing are well known. Vacuum baking of assemblies is commonly performed at temperatures exceeding 600°C to eliminate deeply buried organic contaminants in metals as well as the less well bound water, oxygen and nitrogen. The device design needs to be compatible with high temperature baking. Thus glass constituents ultimately need to be eliminated from the design since they limit baking to temperatures below about 525°C. Unfortunately, the present DMFE devices have been provided to us with glass-to-metal feedthrough's for the cathode and extraction electrode contacts. We plan to use this assembly for the preliminary testing of the concepts, but will move to all metal-ceramic design for future devices. This will take more design and fabrication time than is available in this Phase I contract.

The second issue is related to free space and surface breakdown both inside and outside the device. Traditional values for free space breakdown require about 0.003 inches of gap per 1kV of voltage difference. Assuming a maximum anode voltage of 10kV, this requires spacing between anode and focusing electrode near 750 μm, assuming excellent outgassing of materials. Outgassing and the buildup of contaminant gasses within the vacuum housing will cause breakdown to occur at lower operating voltages. Our existing high temperature vacuum ovens are capable of processing components and finished devices at temperatures over 1000°C at pressures below 10⁻⁸ Torr. This should enable deep outgassing of all vacuum components and ensure long lifetime devices.

3.4.6 SUVOS Power Supply

Until we have a better idea regarding the voltage and current requirements for pumping the ESUVOS we will not be able to finalize ideas for the power supply. But to give some idea regarding power supply prospects we illustrate two commercially available miniature high voltage power supplies below in Figure 41.

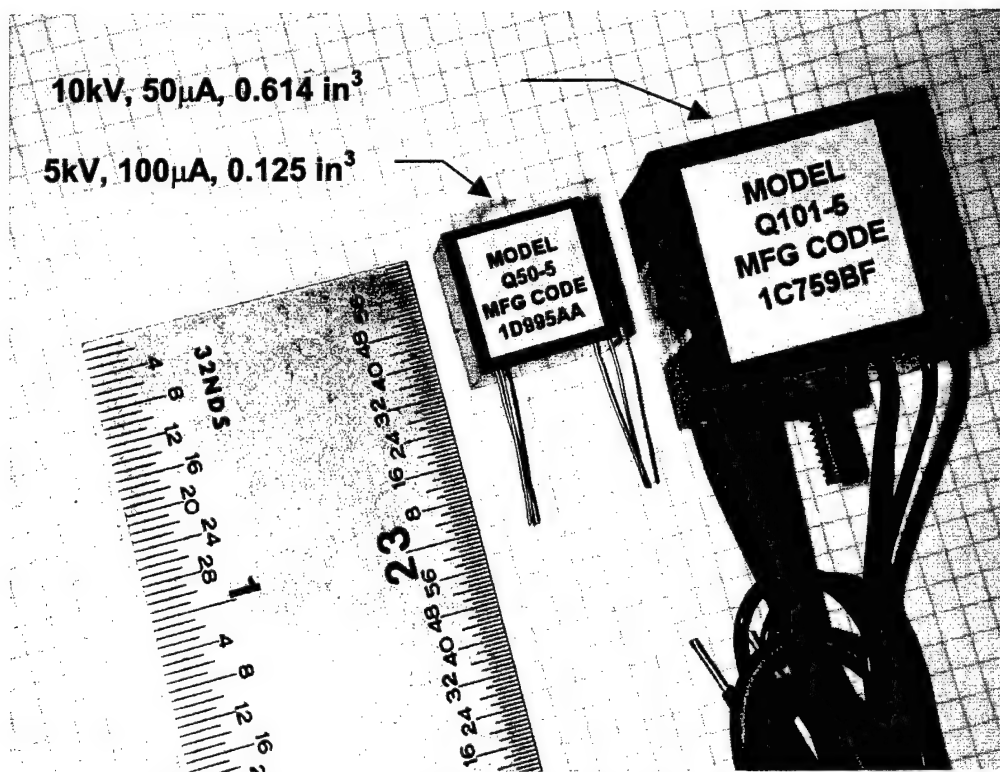


Figure 41. Photographs of two versions of 500 mW power supplies: 5kV and 10kV

We anticipate that the smaller of the two power supplies above will be adequate for pumping MQW AlGaIn devices since the power density expected for stimulated emission is only about 10 kW/cm^2 compared to about 250 kW/cm^2 for bulk material. This power supply (Q50-5) is also similar in size to the planned ESUVOS device and can be packaged together in a miniature package of about $1\text{ cm} \times 1\text{ cm} \times 2\text{ cm}$. The Q50-5 power supply can pump an area about $2\text{ }\mu\text{m} \times 500\text{ }\mu\text{m}$ at the flux level of 50 kW/cm^2 . Power consumption is expected to be between 100 mW and 500 mW for the ESUVOS device.

3.4.7 Laboratory Testbed for ESUVOS

In order to test the e-beam focusing design as well as AlGa_N target cooling and other features of the miniature ESUVOS we have built a laboratory test apparatus that is shown below in Fig. 42 during construction.

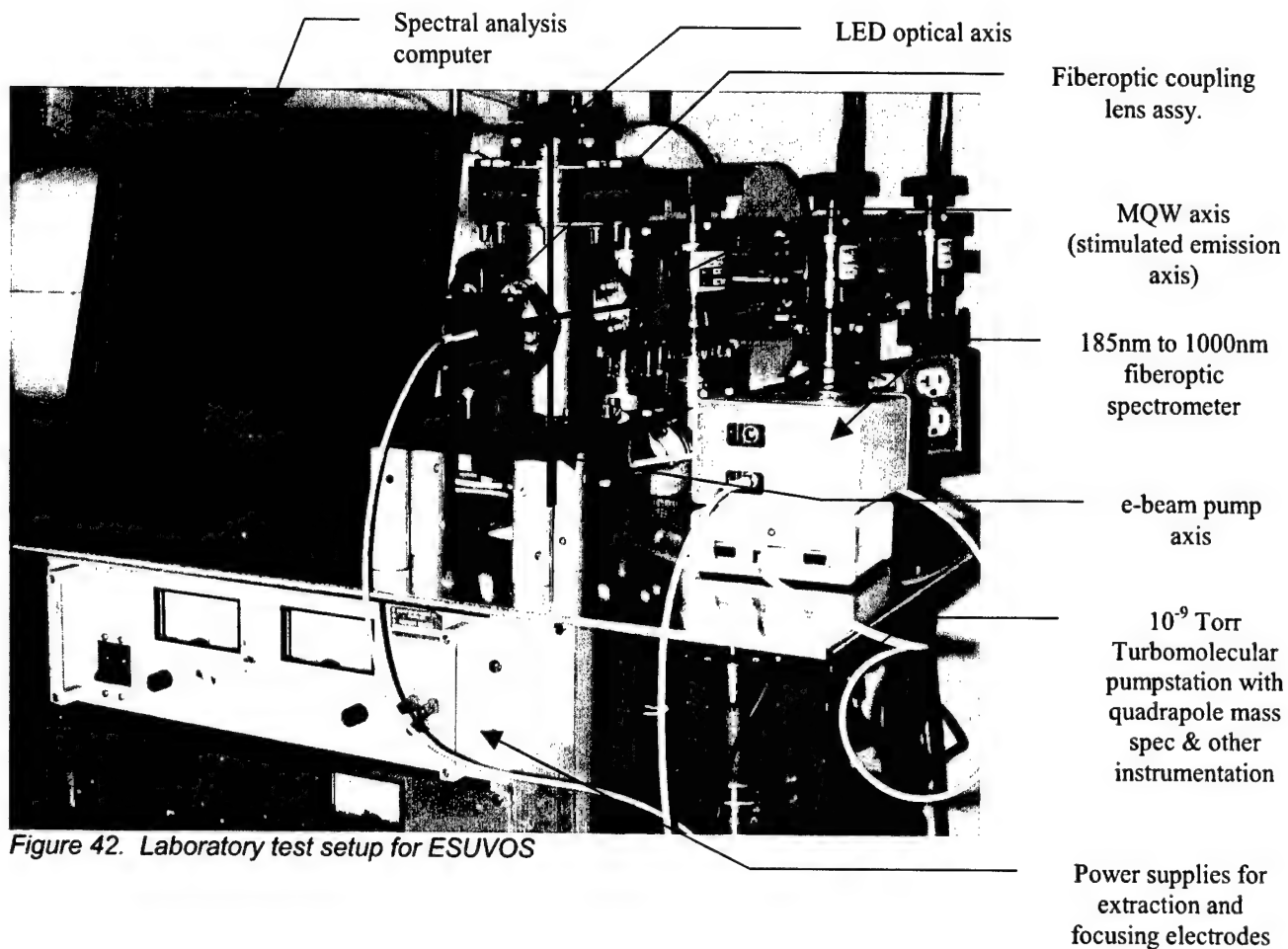


Figure 42. Laboratory test setup for ESUVOS

The above ESUVOS apparatus was added on to one of our high temperature vacuum outgassing process stations. This process station operated in the 10⁻⁹ Torr range and is fitted with a quadrupole mass spectrometer and other instrumentation to enable monitoring of the processing of the ESUVOS. This apparatus allows us to rapidly change our focusing and anode electrode shapes and spatial relationships since each element is mounted on separate posts within the vacuum cross. The posts are connected to high voltage vacuum feedthroughs to enable independent variation of all potentials.

The AlGa_N target is mounted on an anode located at the intersection of the vacuum cross shown above. This enables optical access to both edge and surface emission from the AlGa_N sample. Sapphire windows are located on the top and front side of the vacuum cross. The diamond microtip field emission (DMFE) array source is located below the AlGa_N target with focusing electrode and anode below the AlGa_N target. Edge emission and surface spectral emission can be simultaneously monitored using

an Ocean Optics dual channel UV fiberoptic spectrometer with high NA collection optics. Resolution of this spectrometer is less than 1nm, providing adequate resolution to measure line narrowing resulting from stimulated emission.

Another view of the laboratory device is shown below.

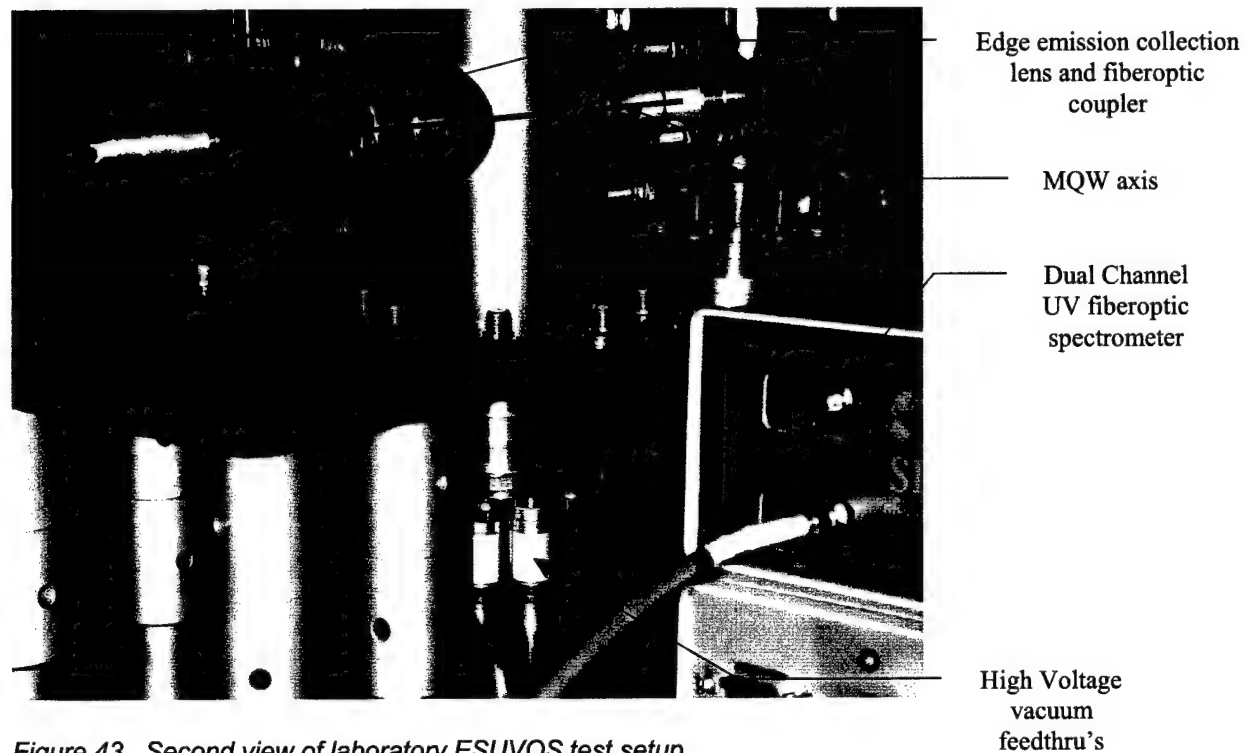


Figure 43. Second view of laboratory ESUVOS test setup

3.5 Optical Detection and Identification of Biological Agents

Raman scattering and fluorescence measure properties of chemical bonds. Chemical bonds can, in turn, be used to infer the presence of specific chemicals. And the presence of specific mixtures or ratios between chemicals can, in turn, be used to infer the presence of specific biological agents. Specifically, spectroscopic marker bands associated with nucleic and aromatic amino acids, dipicolinic acid and other markers all have unique Raman and fluorescence signatures. The ability to optically discriminate microbes from complex backgrounds and classify them, with low false alarm rates, depends on the ability of a proposed technique to accurately measure and relate spectroscopic chemical signatures to essential features of the biological agents under investigation. Low false alarm rates depend strongly on the excitation and observation wavelengths employed, which is true for all optical techniques being proposed. Our focus is on UV resonance Raman and laser induced native (resonance) fluorescence spectroscopy because we believe these techniques are the only viable non-contact optical techniques that could be deployed in miniature, robust, inexpensive packages.

Interpretation of the Raman spectra of macromolecular assemblages, such as biological microorganisms having enormous numbers of degrees of freedom, would appear at first estimate to be extremely challenging. The number of degrees of freedom and subsequent number of Raman bands of a molecule is equal to $3N-6$ for non-linear molecules and $3N-5$ for linear molecules. For molecules with large numbers of atoms, such as biopolymers and mixtures of biopolymers such as occur in living cells, this would indicate a very large number of Raman modes leading to the inability to distinguish any features that could be used as chemical taxonomic markers identifying a particular species or subspecies. Fortunately most biological materials have repeating functional groups (nucleic acid base pairs and aromatic amino acids) that are highly degenerate. This leads to Raman spectra with manageable numbers of basic observable bands. And further, when biomolecules are excited within an electronic absorption band, the number of basic observable modes is further diminished to those bands associated with the molecules within the electronic absorption band.

It is not yet clear whether Raman measurements can provide highly robust identification of biological organisms. However, this said, Kummerle, et.al. provided a 97.5% accuracy in identifying 722 unknown yeast isolates from an FTIR vibrational library of 332 yeast strains²⁰. Leblanc et.al. was able to discriminate between 25 different strains of bacteria using native or resonance fluorescence²¹. And we will show here a substantial ability to discriminate among organisms using both UV Raman and UV resonance fluorescence.

²⁰ Kummerle, M., S. Scherer, and H. Seiler, "Rapid and Reliable Identification of Food-Borne Yeast by Fourier-Transform Infrared Spectroscopy", *App. Environ. Microbio.*, Vol.64, pp.2207-2214 (1998)

²¹ Leblanc, L., and E. Dufour, "Monitoring the identity of bacteria using their intrinsic fluorescence", *FEMS Microbio.Lett.*, Vol.211, pp.147-153 (2002)

3.5.1 Background: Raman vs Fluorescence

Raman scattering is, in general, a very inefficient process. Normal Raman scatter cross-sections are about 10^{-26} cm² for a major Raman line (1615 cm⁻¹) of a typical microorganism²². Normal Raman occurs when the excitation wavelength is far from an electronic absorption band of the material. If the excitation wavelength is within a major electronic absorption band associated with the 1615 cm⁻¹ Raman band, the scattering signal is "resonance" enhanced by as much as eight (8) orders of magnitude, such that the scatter cross-section improves to about 10^{-18} cm². On the other hand, maximum native or resonance fluorescence cross-sections for the same microorganism, over a 30nm wide bandwidth near the peak of fluorescence is about 10^{-11} cm², a factor of 10^7 improvement over resonance Raman. Resonance fluorescence is clearly much more sensitive than resonance Raman, and the threshold of detection will be much lower for fluorescence than Raman. However, much higher levels of specificity can be obtained with Raman. Resonance bands for nucleic and aromatic amino acids occur in the deep UV between about 220nm and 280nm. When excited at wavelengths less than 250nm, Raman scattering occurs within about 20nm to 30nm above the excitation wavelength. Fluorescence occurs only above about 280nm. Therefore, it is ideal to match UV resonance fluorescence and UV Raman spectroscopy to form an integrated tool for both detection and identification of biological agents since they offer a great combination of sensitivity and specificity and do not share overlapping observation wavebands.

3.5.2 UV Resonance Fluorescence Classification of Bioagents

Many of the chemicals that form the building blocks of microorganisms absorb strongly in the deep ultraviolet and exhibit endogenous, native or resonance fluorescence in the near ultraviolet and blue regions of the spectrum. Resonance fluorescence of these molecules is likely the only technique sufficiently sensitive to discover, *in situ* without any sample preparation, the presence and rough classification of a single or few numbers of microorganisms. It is the only viable method of performing non-contact biological classification of aerosols *in situ*²³ because of the small dwell time for observation in an aerosol stream.

When a molecule is irradiated at an excitation wavelength that lies within the absorption spectrum of that molecule, it will absorb the radiant energy and be activated from its ground state (S_0) to an excited singlet state (S_1), with the electron in the same spin as the ground state. The molecule can then relax back from the excited state to the ground state by giving up excitation energy either nonradiatively or radiatively, depending on the local environment. In a nonradiative transition, relaxation occurs by thermal generation. In a radiative transition, relaxation occurs via fluorescence at specific emission wavelengths. Fluorescence generation occurs in three steps: thermal equilibrium is achieved rapidly (10^{-9} s) as the electron makes a nonradiative transition to the lowest vibrational level of the first excited state; the electron then makes a radiative transition to a vibrational level of the ground state (10^{-7} s); and finally the electron makes

²² Wilfred Nelson, U.Rhode Island, private communications.

²³ Faris, G.W., R.A. Copeland, K. Mortelmans, and B.V.Bronk, "Spectrally resolved absolute fluorescence cross sections for bacillus spores", App.Opt., Vol.36, No.4, pp.958-967, 1 February 1997.

a nonradiative transition to the lowest vibrational level of the ground state²⁴. When there is inter-system crossing, in which the spin of the electron is flipped in the excited state, the time for the radiative transition from the excited state to the ground state is longer because the transition must occur with a spin change. This excited state is termed the triplet state. Radiative transition from the excited triplet state is termed phosphorescence with a decay time constant often in the range of milliseconds²⁵.

Fluorescence emission always occurs at wavelengths longer than the excitation wavelength. Fluorescence cross-sections are a function of both the emission and excitation wavelength. If excitation occurs outside of an absorption band, the cross-section will be low, no matter how low the excitation wavelength. It is possible to select an excitation wavelength to emphasize the contrast or targeted biological agents against a wide array of potential background materials. The fluorescence spectrum of a molecule is generally a mirror image of its absorption spectrum and usually forms in broad bands, dependent on the vibrational, rotational and electronic energy level structure of the atom or molecule and its surroundings.

Figure 44 below shows the molar absorptivity of the major aromatic amino acids²⁶. Note that the molar absorptivity peaks for Trp about 225nm and for Tyr about 230nm. Trp absorption at 225nm is 5 to 10 times stronger than in the traditional excitation wavelength at 280nm. The fluorescence cross-section and related efficiency is similarly higher when excited near their optima (Ref.23). It is a common notion that excitation at shorter wavelengths causes more interference with background materials. This is incorrect as will be shown below. The fluorescence cross-section and subsequent emission intensity is a function of both excitation and emission wavelength. This is illustrated in the following

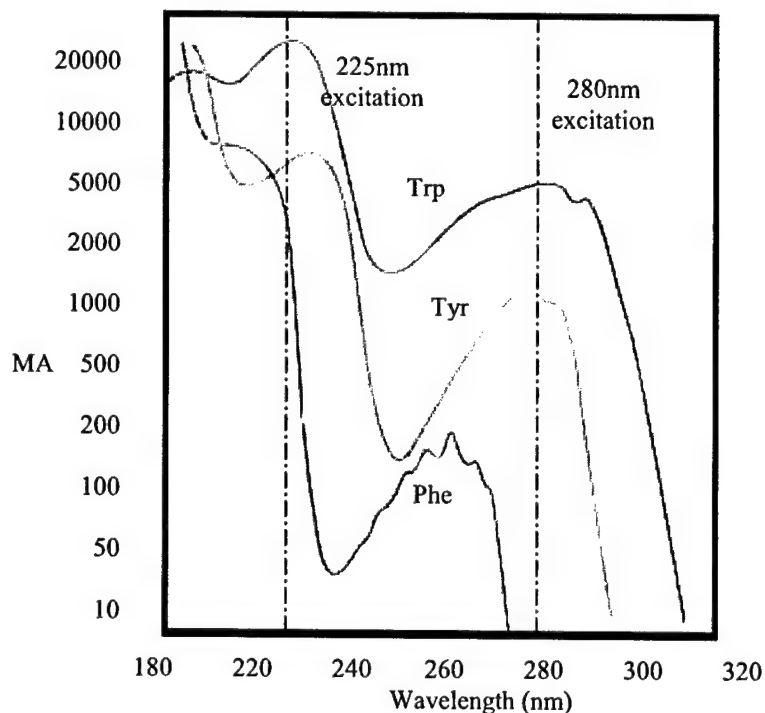


Figure 44. Molar Absorptivity of aromatic amino acids

Excitation-Emission-Matrix (EEM) diagrams.

²⁴ Nirmala Ramanujam, "Fluorescence Spectroscopy In Vivo", in Encyclopedia of Analytical Chemistry, R.A. Meyers (Ed.), pp.20-56, John Wiley & Sons Ltd, Chichester, 2000.

²⁵ J.G. Winans, "Fluorescence and Phosphorescence", in Handbook of Physics, E.U. Condon and H. Odishaw (Ed.), pp.6-131 to 6-157, McGraw Hill Book Co., 1967.

²⁶ Thomas E. Creighton, **Proteins, Structures and Molecular Properties**, (W.H. Freeman and Company, New York, 1993)

EEM diagrams display the fluorescence intensity or cross-section as a function of both excitation and emission wavelength with the iso-intensity shown as contour lines, as illustrated below in Fig. 45 for *Bacillus subtilis* in both the vegetative and spore form.

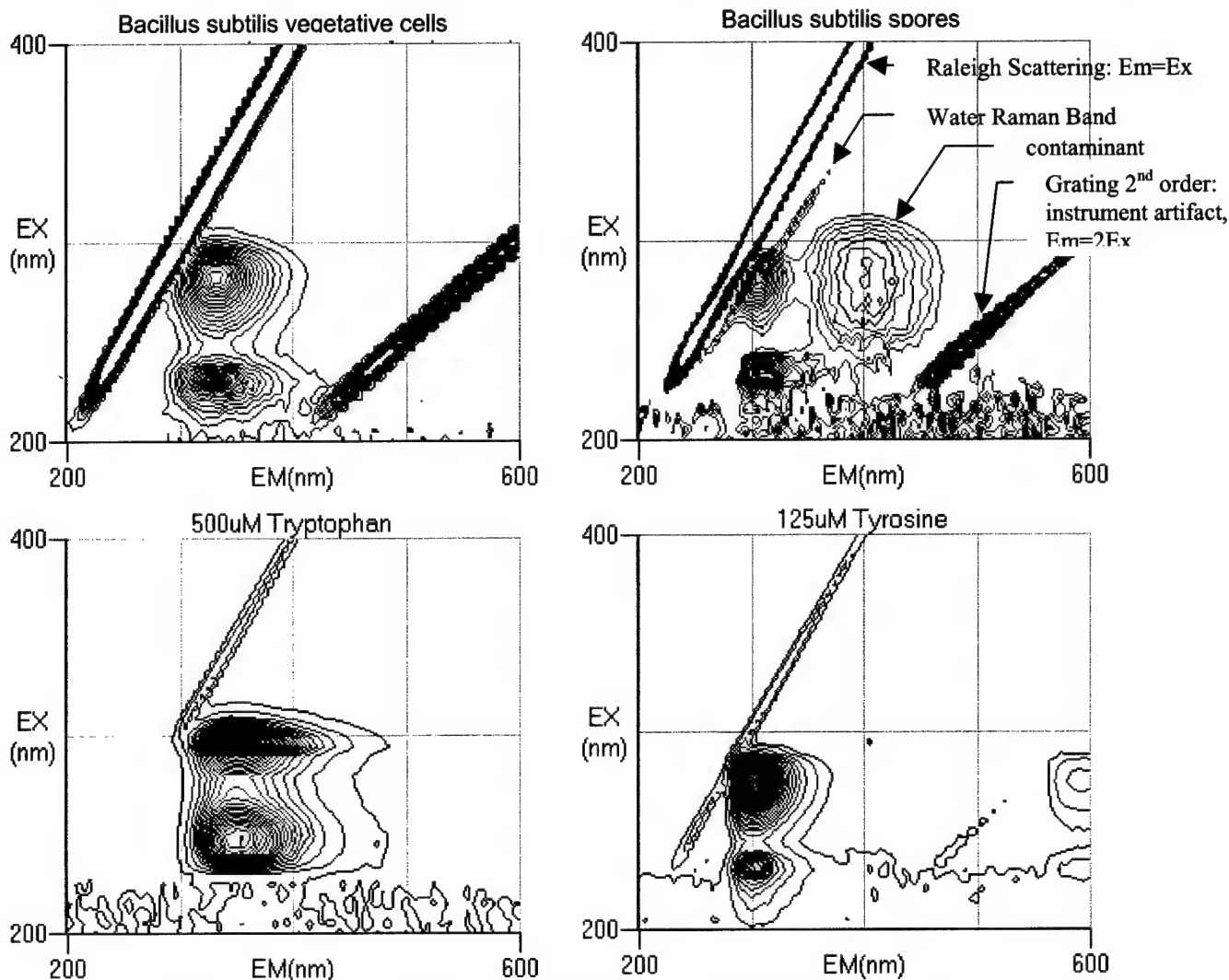


Figure 45. Excitation-Emission-Matrix diagrams for *B. subtilis* spores and vegetative cells.

It is important to note that both the spores the vegetative cells have two optimum excitation wavelengths, one near 230nm and one near 280nm. Emission maxima for both excitation wavelengths are the same, at about 330nm, as expected. *Bacillus subtilis* in spore form ($@10^4$ per ml) are also shown in Fig. 45. **Optimum excitation wavelengths are essentially the same for *B. subtilis* spores and vegetative cells, but the optimum emission wavelength for spores is close to 305nm compared to 340nm for vegetative cells.** This is a clearly distinguishable marker feature of spores. Driks²⁷ shows that the spore coat for *B. subtilis* is dominated by tyrosine, whose fluorescence signature peaks near 305nm rather than the tryptophan, whose peak is near 350nm. This is illustrated in Fig. 45 above by comparison of Trp with vegetative

²⁷ Driks, A., "Bacillus subtilis spore coat", Microbiology and Molecular Biology Reviews, Vol.63, No.1, pp.1-20, Mar. 1999.

forms and Tyr with spore forms of *B.subtilis*. A secondary optima occurring in Fig. 45 at $\text{Ex}=280\text{nm}$ and $\text{EM}=400\text{nm}$ is a result of a denatured alcohol contaminant in the sample. Below in Fig. 46 are the EEM diagrams of several common background materials and minerals.

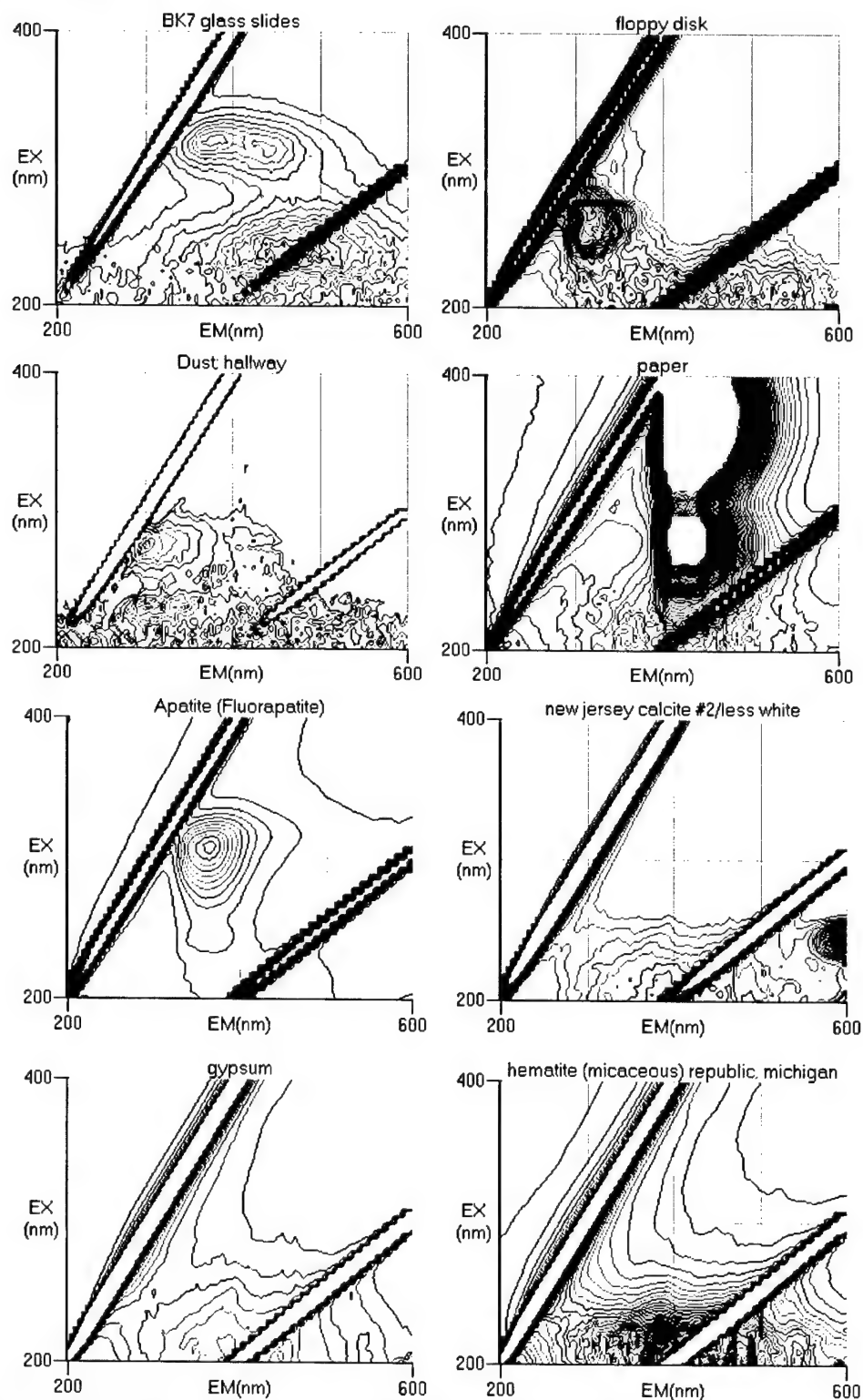


Figure 46. EEM diagrams for several common minerals and background materials

The EEM diagrams in Fig. 46 above illustrate the broad variation in fluorescence fingerprints of many common materials. The EEM fingerprints of any of these materials differ significantly from *B. subtilis* in either the spore or vegetative form shown in Fig. 45. However, when detection is accomplished using a single excitation wavelength, some similarities do exist. When excited near 280nm, the emission spectrum of several plastics is similar to *B. subtilis*. However, when excited near 230nm, the spectrum is distinctly different. In order to obtain high levels of sensitivity a laser source with high power density must be used. In this case only a single excitation wavelength is available. It is of interest to select this excitation wavelength and a set of emission observation wavelengths for which biological agents have the highest possible differential fluorescence against the widest range of background materials. It is clear from the above data that excitation wavelengths deeper than 280nm do not "excite everything" as is commonly believed. Fluorescence cross-sections are very wavelength-specific. Any of several algorithms can be used to optimize the ability to discriminate target and background materials. It is our belief that false alarm rate in the detection of biological-agent-like particles can be significantly improved if excitation occurs near 230nm rather than 280nm.

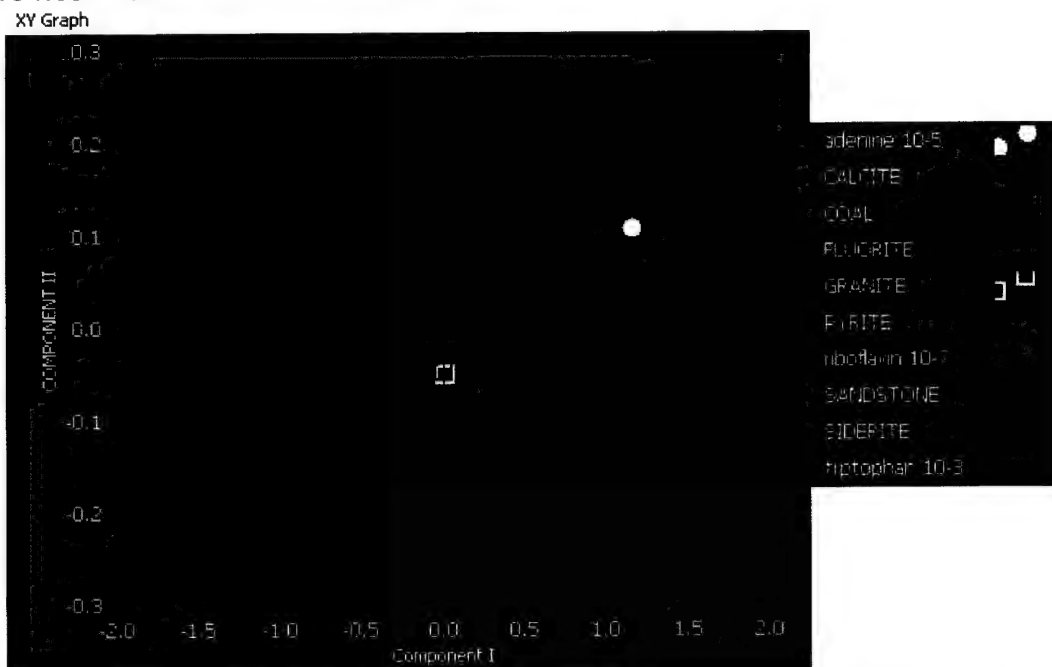


Figure 47. Spectra were acquired on a Hitachi F4500 fluorimeter, excited at 224nm. A filter simulation model determines the fluorescent spectra that will be seen with bandpass filters centered at 280nm, 325nm, 330nm, 350nm, and 370nm with 50 nm wide bands (Gaussian filter shapes are used in the simulation). The banded fluorescence emission spectra attained are run through a PCA algorithm to determine where the mineral spectra (open squares) cluster versus where the organics (closed circles) appear. Using tryptophan, which exhibits one of the largest fluorescence cross-sections of the organics, riboflavin, and adenine as organic examples, definitive separation from the minerals (calcite, coal, fluorite, pyrite, and siderite) and rocks (granite and sandstone) is seen. Of note is the separation of the fluorite from the mineral/rock cluster. This is due to fluorite's visible fluorescence emission, which has little effect on the ability to differentiate it from the organics' fluorescence. (Courtesy R. Bhartia, NASA/JPL)

Figure 47 above illustrates the ability of laser induced resonance fluorescence to distinguish chemicals associated with spores and a range of mineral materials using Principle Component Analysis. As part of an upcoming NASA-sponsored program, Photon Systems is developing very fast data processing algorithms to identify organic classification of particles detected in water or on surfaces. Computation time goals are of the order of 10ns per identification decision.

3.5.3 UV Resonance Raman Identification of Biological Agents

Photon Systems has been developing miniature deep UV Raman instruments and associated deep UV lasers for several^{28,29} in collaboration with Professors Wilfred Nelson of University of Rhode Island and Sanford Asher at University of Pittsburgh and NASA/JPL/Center for Life Detection. Professor Asher is the father of UV resonance Raman spectroscopy (UVRRS) and Prof. Nelson is the father of the use of UVRRS to identification of microorganisms.

Raman spectroscopy has been demonstrated to be a highly selective measurement technique that requires no sample preparation, is non-contact, and is non-destructive³⁰. Many biological materials and other background materials emit fluorescence, providing an undesirable background signal that masks the Raman emission unless the laser excitation wavelength is below about 250nm. Fluorescence resulting from excitation below 250nm has a large Stokes shift to wavelengths above 280nm, providing a fluorescence-free region above the excitation wavelength in which to measure Raman emission with no background³¹. A four thousand wavenumber Raman shift corresponds to about 25nm at 250nm. In addition, excitation in the 250nm range is within the strong absorption bands of nucleic acid, providing resonance enhancement of the Raman scattering by as much as eight orders of magnitude. Below are the major Raman band assignments for key nucleic and aromatic acids and dipicolinic acid, a marker for bacterial spores.

²⁸ Sparrow, M.C., J.F. Jackovitz, C.H. Munro, W.F. Hug, and S.A. Asher, "A New 224nm Hollow Cathode UV Laser Raman Spectrometer", *J. App. Spectroscopy*, Vol. 55, No. 1, Jan 2001.

²⁹ Storrie-Lombardi, M.C., W.F.Hug, G.D.McDonald, A.I. Tsapin, and K.H.Nealson, "Hollow Cathode Ion Lasers for Deep Ultraviolet Raman Spectroscopy and Fluorescence Imaging", *Review of Scientific Instruments*, Dec. 2001

³⁰ Cary, P.R. (1982) *Biological applications of Raman and resonance Raman spectroscopies*, Academic Press, New York.

³¹ Asher, S.A., private communications and many publications. N.Cho and S.A. Asher, "UV resonance Raman studies of DNA-Pyrene interactions", *J.Am. Chem.Soc.* 115, pp.6349-6356, 1993

Table V. Basic Raman band assignments for components of biological agents^a

Molecule	Basic Raman Band Assignment ¹ (Ref. 29)
Tryptophan	<u>757-762</u> : symmetric ring stretch of benzene and pyrrole <u>877-880</u> : in-plane deformation 1006-1016 : symmetric ring stretch of benzene and pyrrole <u>1340-1350</u> : a pyrrole ring vibration 1549-1555 : symmetric stretching of the indole ring <u>1614-1622</u> : phenyl ring vibration
Tyrosine	830-832: Fermi resonance doublet 850-853: symmetric ring stretch 1178-1180 : in-plane CH stretch 1209-1210: symmetric stretch 1613-1617 : in-plane ring stretching
Guanine	<u>1322-1326</u> : purine ring bonds (N7C8s; C8Hb) 1485-1489 : purine ring bonds (C8Hb; C8N9, N7C8s) 1575-1580: ring mode stretching (N3C4, C4C5, C5N7s) 1603: in-plane bending and ring stretching (N1Hb, C2Ns)
Adenine	1336-1339 : purine ring bonds (C5N7, N7C8s) 1482-1485: purine ring bonds (C4N9s, C8Hb) 1580-1581: ring mode stretching (C4C5, N3C4s)
Cytosine	1527-1528 : ring stretching mode (N3C4, N1C2s) 1650: in-plane bending and ring stretching (C2=O, C2N3s)
Dipicolinic Acid	1017, 1195, 1396, 1446

^aRaman band frequencies are in cm^{-1} units. Assignments, frequency ranges and nomenclature are from experimental and model compound studies using excitation between 223-229nm and 244-248nm. Nucleic acid studies employed nucleotides, deoxynucleosides, or the duplexes poly (rA)poly(rU) and poly (dG-dC). Abbreviations signify Raman stretching and bending modes. The most prominent bands are in bold. Regions exhibiting significant activity in the present study are underlined.

It has been clear for several years that unique ultraviolet resonance Raman spectral signatures can reliably be detected in as few as 20 bacterial cells with low power consumption and low photon flux levels (Nelson, 1993³²; Nelson, et.al³³, 1993; Chadha, et.al., 1993³⁴). In fact, UVRR has made possible the detection and characterization of single cells.

Taxonomic Raman Marker Bands

A summary of the major taxonomic marker bands of highly degenerate functional groups occurring within microorganisms is shown below in Table III.

Table VI. Major Taxonomic Raman marker bands for biological agents

Material	Raman Band Locations					
Tryptophan	753	879	1011	1353	1555	1615
Tyrosine	831	852	1180	1210		1615
Guanine				1320 1365	1485	1577 1603
Adenine				1337	1485	1580
Cytosine					1530	
Dipicolinic Acid			1017	1195	1396	1446

³² Nelson, W.H. (1993) *Rev Sci. Inst.* (11):3088-3093

³³ Nelson, W.H., Manoharan, R., and Sperry, J.F. (1992) *Appl. Spect. Rev.* 27(1), 67

³⁴ Chadha, S., Nelson, W.H., Sperry, J.F. (1993) *Rev. Sci. Inst.* (11):3088-3093

Identification of biopolymers or organisms using UV Raman spectroscopy depends on the ability to produce interpretable, reproducible spectra. DNA and cell surface antigens are the most attractive targets as potential markers for cellular or bacterial identification. Identification of organisms using UV Raman spectroscopy has focused on the ratio of a few taxonomic marker bands (Ref.33). These band markers are based on ratios of tryptophan and tyrosine and DNA base pairs that can be characteristic of an organism. As mentioned previously, most biological materials have repeating functional groups that are highly degenerate. These include nucleic acid base pairs and aromatic amino acids. These repeating units have Raman spectra that are very similar to the spectra of the monomers upon which they are based. Raman spectra of *B. cereus* in several forms is shown below in Fig. 48 in using 242nm excitation: vegetative, spore and germinated spore (Ref.33). Major Raman marker bands are shown at 1019 cm^{-1} , 1485 cm^{-1} , 1530 cm^{-1} , 1555 cm^{-1} , and 1615 cm^{-1} . The measurement bandwidth illustrated is about 25 cm^{-1} .

Bacteria can be characterized as Gram positive versus Gram negative based on the $1555\text{ cm}^{-1}/1615\text{ cm}^{-1}$ intensity ratio. Gram negative bacteria have a much higher

ratio of the tryptophan intensity at 1011 cm^{-1} or 1555 cm^{-1} compared to the tyr+trp intensity at 1615 cm^{-1} . In general, this ratio is described as the intensity in broad spectral regions centered near the 1555 cm^{-1} and 1615 cm^{-1} Raman bands. However, the exact position, center of gravity, band width, and other features of each band can provide more detailed identification of bacteria. However, the relationships are presently unknown. It is believed that these marker bands primarily describe the surface composition of an organism.

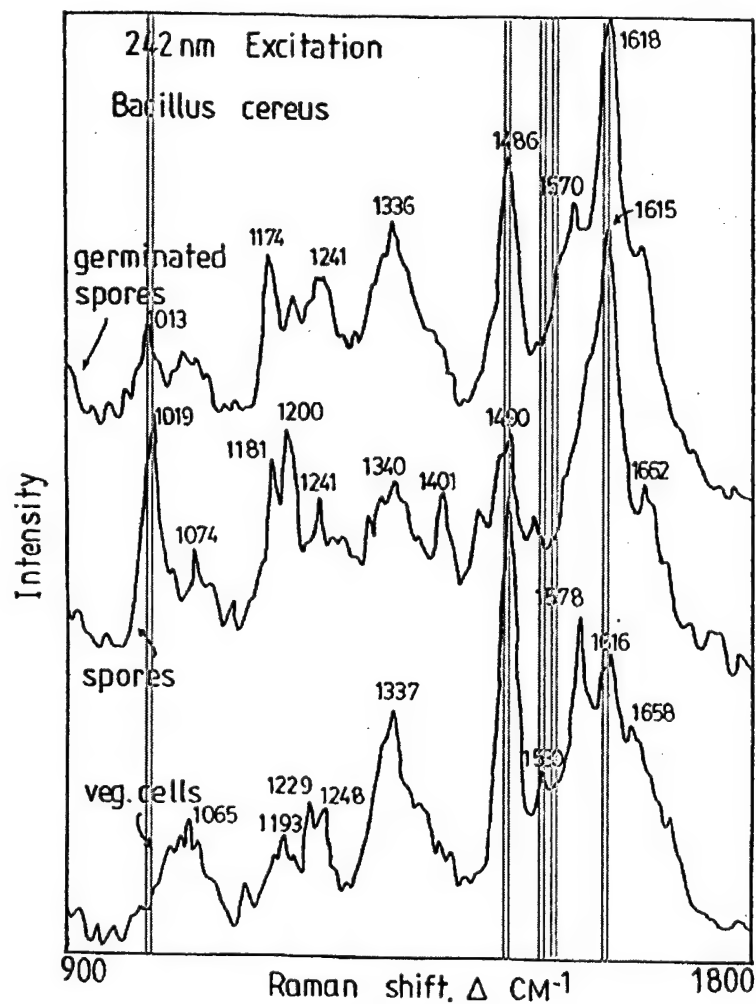


Figure 48. Resonance Raman spectra of *B. cereus* in various forms(Ref.33)

Within Gram positive organisms such as spores, or vegetative cells there is further sub-classification G+C percentage. This is determined by the $1530\text{ cm}^{-1}/1485\text{ cm}^{-1}$ Raman band intensity ratio. The intensity of the 1485 cm^{-1} peak is taken as closely proportional to the total amount of nucleic acid on a molar basis (DNA + RNA) in the cell. The intensity of the peak at 1530 cm^{-1} can be assumed to be proportional to the moles of cytosine in the nucleic acids. It follows that the mole fraction of G+C in the bacteria should be proportional to the ratio of the 1530 cm^{-1} and 1485 cm^{-1} peaks.

Following is a graph of the $1530/1485\text{ cm}^{-1}$ ratio versus the known percentage of G+C of DNA in 14 different bacterial species grown on TSA and in TSB, respectively (Ref.33). The peak intensity ratios versus molar percent G+C are linear dependent, as shown in Fig. 49.

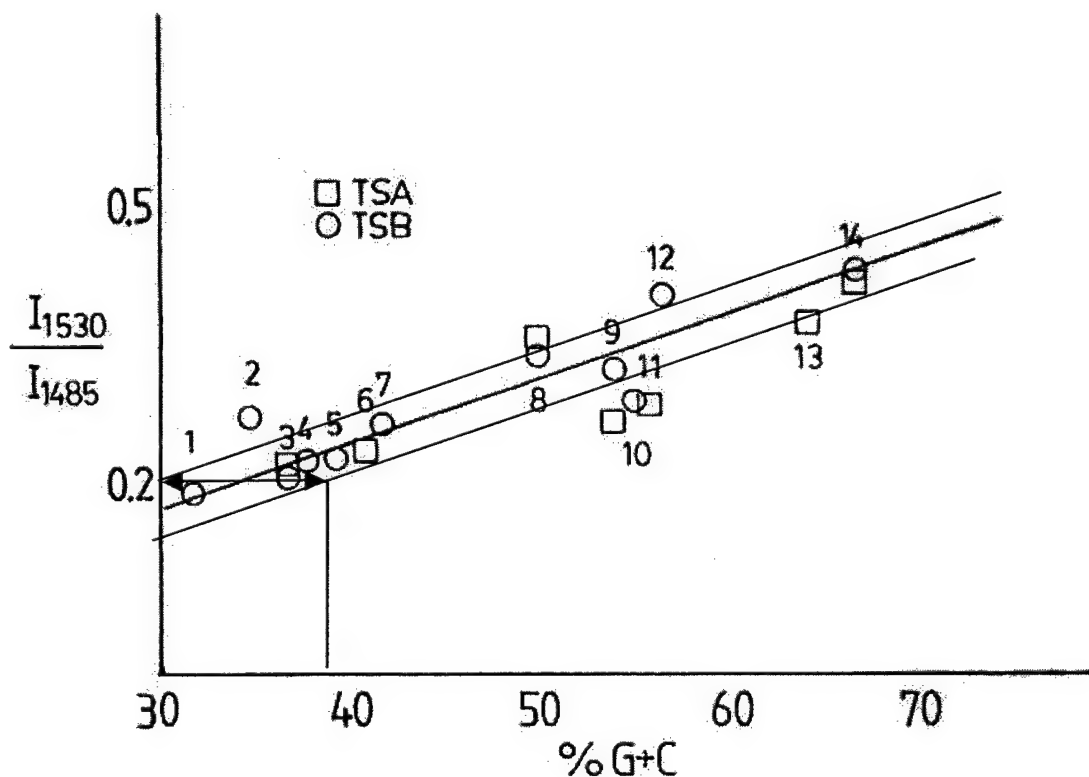


Figure 49. Plot of $1530\text{ cm}^{-1}/1485\text{ cm}^{-1}$ versus known G+C for 14 bacterial species. 242nm excitation. (Adapted from Ref.33)

Three lines are shown in Fig. 49 which represent the mean and \pm one standard deviation of the data. This preliminary estimate illustrates the potential to identify an organism within about ± 3 to ± 5 mole percent G+C. In combination with identification of the Gram polarity and whether the organism is a spore, the G+C content can provide significant specificity in identification of biological agents. The organisms employed in Fig. 49 are tabulated below in Table VII.

Table VII. DNA mole fraction for Guanine + Cytosine for bacteria in Fig. 49

Plot No.	Organism	Mole% G+C	Gram	Spores	Virulence class ^g
	<i>Clostridium botulinum</i>	28.2 ⁱ	+	X	2
	<i>Rickettsia prowasecki</i>	28.9 ⁱ	-		3
	<i>Staphylococcus aureus</i>	32.8 ^b	+		2
1	<i>Bacillus cereus</i>	32 ^a	+	X	1
2	<i>Enterococcus faecalis</i>	34-36 ^a 37.5 ^b	-		1
	<i>Staphylococcus simulans</i>	34-38 ^a	+		1
	<i>Bacillus anthracis</i> Ames	35.2 ^b	+	X	2
	<i>Streptococcus agalactiae</i>	35.5 ^b	+		1
4	<i>Proteus vulgaris</i>	36-40 ^a	-		1
3	<i>Bacillus magaterium</i>	37 ^a	+	X	1
5	<i>Proteus mirabilis</i>	39.5 ^a	-		1
6	<i>Bacillus subtilis</i>	41 ^a	+	X	1
7	<i>Acinetobacter calcoaceticus</i>	42 ^a	-		2
	<i>Bacillus subtilis</i>	43.5 ^b	+	X	1
	<i>Shewanella oneidensis</i> MR1	45.9 ^b	-		1
	<i>Yersinia pestis</i> .	47.6 ⁱ	-		3
	<i>Vibrio cholerae</i>	47.6 ⁱ	-		3
8	<i>Escherichia coli</i> , K12-MG1655	50.7 ^b	-		2
	<i>Shigella dysenteriae</i>	50 ⁱ	-		2
	<i>Samonella tphi</i>	52.1 ⁱ	-		2
9	<i>Enterobacter aerogenes</i>	54.3 ^a	-		1
10	<i>Alcaligenes faecalis</i>	54.8 ^a	-		1
11	<i>Enterobacter cloacae</i>	55.4 ^a 57.2 ^b	-		1
12	<i>Aeromonas hydrophila</i>	55.7 ^a	-		1
	<i>Brucella suis</i> 1330	57.2 ^b	-		3
	<i>Brucella melitensis</i>	57.2 ^c	-		3
	<i>Aeromonas hydrophila</i>	59-62 ^c	-		1
	<i>Pseudomonas putida</i>	61.4	-		1
13	<i>Pseudomonas aeruginosa</i>	64 ^a , 66.4 ^b	-		1
14	<i>Micrococcus luteus</i>	66.3 ^a	+		1
	<i>Alcaligenes faecalis</i>	66.7-69.9 ^c	-		1
	<i>Burkholderia pseudomallei</i>	68.06 ⁱ	-		3

a=A.I.Laskin & H.A.Lechevallier(eds), CRC Handbook of Microbiology, Vol.II, CRS Press, Cleveland, 1973. b=tigr, i=Sanger Inst.

Biological Agent Identification Specificity

One possible detection and identification strategy for biological agents using laser induced resonance fluorescence and UV Raman spectroscopy is as follows:

- a. Determine if a particle is biological or non-biological based on laser induced resonance fluorescence measured in the 300nm region.
- b. If particle is biological, measure the relative UV Raman intensity at five (5) Raman bands centered at 1017 cm^{-1} , 1485 cm^{-1} , 1530 cm^{-1} , 1555 cm^{-1} and 1615 cm^{-1} .
- c. Determine if the particle is Gram positive or negative based $1555\text{ cm}^{-1} / 1615\text{ cm}^{-1}$ ratio.
- d. Determine if the particle is a spore based on the $1017\text{ cm}^{-1} / 1615\text{ cm}^{-1}$ ratio.
- e. Determine the GC% based on the $1530\text{ cm}^{-1} / 1485\text{ cm}^{-1}$ ratio.

Measurement of the Raman scattering in only five (5) broad ($\approx 40\text{ cm}^{-1}$) bands **provides knowledge of the: Gram polarity; form of organism; and G+C percent.** These measurements can be made rapidly and correlated using any of several artificial neural net or PCA/PCO algorithms to give a relatively high degree of confidence in identifying organisms within a narrow range. These measurements could be made in sub-second time scales and possibly as short as a millisecond or faster.

Using this fast and simple 5-band Raman technique, it would appear that it is unlikely this method would be able to specifically differentiate *B. anthracis* against a background containing a wide range of other similar spore interferants since the detection accuracy corresponds to only about $\pm 4\%$ in G+C concentration. The closest spore to *B. anthracis* at GC=35.2% is *B. cereus* at 32% ($\Delta=3.2\%$) and *B. magisterium* at 37% ($\Delta=1.8\%$). All three are spore formers and all are Gram positive. So none of the discriminators would have differentiated between these organisms with a low false alarm rate. However, this fast method will probably enable discrimination of *B. subtilis* from *B. anthracis*. In addition, this method would be able to discriminate anthrax from a wide range of other bacterial spores and other microorganisms and identify them within a small range.

The above measurements and correlations were done at an excitation wavelength of 242nm. The effect of employing other excitation wavelengths is shown in Fig. 50 below. It is clear from this figure that excitation wavelengths need to be between 230nm and about 255nm. Excitation wavelengths below this range would not clearly distinguish the dipicolinic acid peak at 1019 cm^{-1} . Wavelengths above 255nm would run into fluorescence background for high Raman shift marker bands.

There are many UV Raman spectroscopic options that have yet to be evaluated to reduce the false alarm rate in identifying *B. anthracis* or other virulent microorganisms. The fast and simple approach described above does not take advantage of the much larger wealth of information contained in UV Raman spectra. Substantial differences in taxonomic marker band intensity, peak position, center of gravity, and band shape occur for each of the basic Raman marker bands. These are a result of environmental and

conformational differences between organisms as well as more subtle compositional differences. In addition, there are other Raman marker bands that are clearly measurable which may give further discrimination to microorganism identification. In order to provide a higher level of biological agent specificity, higher resolution Raman spectra would be required. A reasonable way to triage a target would be to follow the laser induced resonance fluorescence and broadband UV resonance Raman with high resolution UV resonance Raman. Each of these techniques is successively more time consuming, less sensitive and more specific. At present there is no clear model to provide higher specificity based on more subtle nuances of the Raman spectra such as peak position or center of gravity variations due to difference in microorganisms. This is the subject of a further study in Phase II of this program.

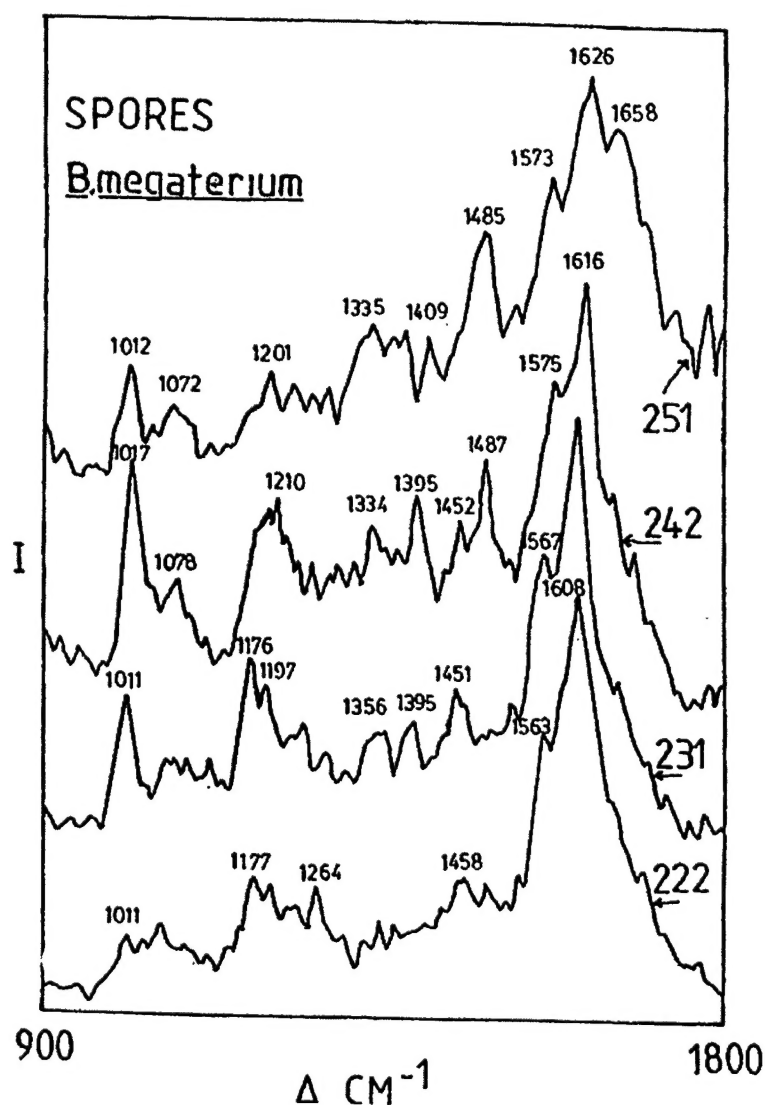


Figure 50. Effect of excitation wavelength on Raman spectra of *B. megaterium*(Ref.33)

UV MicroRaman Instrument: General Specifications

Photon Systems is developing an ultra-sensitive, fully integrated, compact, light weight and low power consumption UV resonance Raman instrument for use in non-contact, non-destructive identification of biological agents and other organic and inorganic materials. Details of this technology are proprietary and will be disclosed after a patent has been submitted. The instrument has the following specifications.

- Compact: <500cc
- Light weight <1kg
- Low Power consumption: <1W
- Excitation wavelength: 230nm to 250nm
- Raman spectral range: 500 cm^{-1} to 3500 cm^{-1}
- Spectral resolution: <40 cm^{-1} raw, <20 cm^{-1} processed
- Spectral tuning: computer controlled sequential or non-sequential Raman bands
- Detection gain: 10^7
- Working distance >5cm
- Fully integrated: Contains laser Raman spectrometer and all operating and control electronics

4.0 Conclusions and Recommendations

Ultraviolet excited resonance fluorescence and resonance Raman are powerful instrumental methods for detection, classification and identification of biological agents used in biological warfare. UV resonance fluorescence is currently recognized as the most sensitive tool for detection and rough classification of biological agents. We believe that higher levels of specificity and lower false alarm rates are possible with more optimum choices in excitation and detection wavelengths. Current excitation wavelength goals are at 280nm. We believe there is an opportunity to lower false alarm rates at excitation wavelengths closer to 230nm. In addition, with a more optimum choice of detection wavebands, we believe specificity can be improved.

UV resonance Raman spectroscopy has long been touted as a technique that can provide much higher levels of specificity than fluorescence without excessive loss of sensitivity. We believe we have quantitatively demonstrated that a considerable level of biological agent identification is possible with this technique. We also believe we have shown that even higher levels of specificity can be achieved with UV resonance Raman spectroscopy in the future.

The primary goal of this Phase I SBIR has been to demonstrate feasibility of a semiconductor laser with output in the deep UV. We have demonstrated strong stimulated emission at 272nm with emission linewidth collapse from 16nm to 4nm and corresponding increase in output of five orders of magnitude. In addition, we have designed and fabricated complete devices that are yet to be tested.

We believe we have more than satisfied the objectives of this Phase I SBIR grant and recommend and request funding Phase II of this project. During Phase II we will have fully functional, deep UV, semiconductor lasers operating at less than 250nm with emission linewidth less than 40 cm^{-1} . We will also have a functional microRaman spectrometer system employing the new laser, integrated into a package less than 500cc, weighing less than 1kg, and consuming less than 1W of power.

5.0 Distribution List

- a. Director,
Defense Advanced Research Projects Agency
Attn: MTO (LTC John Carrano)
3701 North Fairfax Drive
Arlington, VA 22203-1714
 - b. U.S. Army Aviation and Missile Command
Attn: AMSAM-RD-WS-DP-SB 9 (Gayla McMichael, Tech Monitor)
Bldg. 7804, Room 205
Redstone Arsenal, AL 35898
 - c. Commander, U.S. Army Aviation & Missile Command
Attn: AMSAM-RD-OB-R
Bldg. 4484, Room 204
Redstone Arsenal, Alabama 35898-5241
 - d. Commander, U.S. Army Aviation & Missile Command
Attn: AMSAM-RD-WS
Bldg. 7804, Room 247
Redstone Arsenal, Alabama 35898-5248
 - e. Director
Defense Advanced Research Projects Agency
ATTN; CMO/SBIR
3701 North Fairfax Drive
Arlington, VA 22203-1714
 - f. Director
Defense Advanced Research Projects Agency
ATTN; OMO/DARPA Library
3701 North Fairfax Drive
Arlington, VA 22203-1714
 - g. Defense Technical Information Center
ATTN; Acquisitions/DTIC-OCP, Rm-815
8725 John J. Kingman Rd., STE 0944
Ft. Belvoir, VA 22060-6218
-